CONF-820853--4

CONF-820853--4

DE83 007864

VUV SPECTROSCOPY OF RARE GAS VAN DER WAALS DIMERS*

P. M. Dehmer and S. T. Pratt
Argonne National Laboratory, Argonne, Illinois 60439

To appear in
Proceedings of the NATO Advanced Study Institute on
Photophysics and Photochemistry in the Vacuum Ultraviolet
Lake Geneva, Wisconsin
16-27 August 1982
(D. Reidel Publishing Co., Dordrecht, Holland, 1983)

---

* Work supported by the U.S. Department of Energy and the Office of Naval Research.

I. INTRODUCTION

It is well known that ground state rare gas atoms repel each other except for van der Waals forces, which lead to weak molecular binding in all of the homonuclear and heteronuclear dimers except possibly He_2.[1] Removal of the outermost electron, which is antibonding in character, leads to a stable ground ionic state for all of the dimers. Several of the excited ionic states are bound as well, although, in general, the dissociation energies of the excited states are much smaller than that of the ground state. The addition of an electron in a Rydberg orbital to an ion in one of the bound states may result in a bound Rydberg state; however, little is known about the stable excited states of the neutral rare gas dimers, except for those molecular states which arise from the lowest atomic resonance states (i.e. the molecular excimer states). A notable exception is the detailed multichannel quantum defect theory analysis of the Rydberg states in He_2 presented recently by Ginter and Ginter.[2]

With this in mind, we have undertaken a systematic study of the photoionization spectra of the homonuclear and heteronuclear rare gas dimers in order to better understand the nature of the bonding in the Rydberg states and ions of these molecules. We have obtained results for Ar_2,[3,4] Kr_2,[5] Xe_2,[6] NeAr, NeKr, NeXe,[7] ArKr, ArXe, and KrXe.[8] Of the remaining dimer species (Ne_2 and the He-rare gas dimers), only Ne_2 has been studied using photoionization mass spectrometry.[9]

The results of the present series of experiments provide information both on the excited states of the neutral dimers and on the ground and excited states of the dimer ions. Using the data obtained in these mesurements, we are able to compile for the first time a nearly complete list of ground state dissociation energies for the homonuclear and heteronuclear rare gas dimer ions. Somewhat less complete results are obtained for the excited states of these species. The observed trends in binding energy provide an excellent example of the systematic changes that occur as a result of changes in atomic orbital energies, polarizability, and internuclear distance, and these trends can be explained qualitatively in terms of simple molecular orbital theory.

II. GENERAL BACKGROUND

Since the potential energy curve of a Rydberg state is built on, and therefore closely resembles, its ionic convergence limit, a knowledge of the bonding in the ground and excited states of the dimer ions is required to understand the bonding in the Rydberg states. A homonuclear rare gas dimer ion X_2^+ has a bound ${}^2\Sigma^+_{1/2u}$ ground state and five excited states, all of which are repulsive except for a small polarization minimum at large internuclear distance (R).[1] At small R, a molecular orbital description of the states is appropriate, and the states are labeled, in order of increasing energy, ${}^2\Pi_{3/2g}$, ${}^2\Pi_{1/2g}$, ${}^2\Pi_{3/2u}$, ${}^2\Pi_{1/2u}$, and ${}^2\Sigma^+_{1/2g}$. At large R, the states are labeled according to case c coupling rules and their ordering may be different, but must be consistent with the appropriate non-crossing rules. Wadt[10] has shown that for $Ar_2{}^+$, $Kr_2{}^+$, and $Xe_2{}^+$ a crossing occurs at intermediate R between the ${}^2\Pi_{1/2g}$ and ${}^2\Pi_{3/2u}$ states. The ground and first three excited states given above dissociate to $X({}^1S_0) + X^+({}^2P^o_{3/2})$, and the remaining two excited states dissociate to $X({}^1S_0) + X^+({}^2P^o_{1/2})$. Figure 1 gives a schematic potential energy diagram for X_2^+ in which the dissociation energies and spin-orbit splitting are patterned after those of Xe_2^+.[11] Following Mulliken's convention,[1] the states are labeled A ${}^2\Sigma^+_u$, B ${}^2\Pi_g$, C ${}^2\Pi_u$, and D ${}^2\Sigma^+_g$. Huber and Herzberg[12] have renamed the ground state X, but have not changed the notation of the excited states.

By analogy with the above, and from recent theoretical calculations by Bender and Winter[13] on the potential curves of the heteronuclear dimer ions XY^+ (where X has the greater ionization potential), it is possible to construct a schematic potential energy diagram for the heteronuclear ions. A total of six ionic states remain, but now the three lower energy curves dissociate to $X(^1S_0) + Y^+(^2P^o_{3/2 \text{ or } 1/2})$ and the three higher energy curves dissociate to $X^+(^2P^o_{3/2 \text{ or } 1/2}) + Y(^1S_0)$. Representative potential energy curves for XY^+ patterned after the $ArKr^+$ curves calculated by Bender and Winter are shown in Figure 2. Again, the ground ionic state is the most strongly bound. (For HeY^+, only one state dissociates to $He^+(^2S_{1/2}) + Y(^1S_0)$, and this state is more strongly bound than the ground ionic state in $HeAr^+$, $HeKr^+$, and $HeXe^+$.) By analogy with the homonuclear dimers, we label the ground $^2\Sigma^+_{1/2}$ state A, the two $^2\Pi$ states B and C in order of increasing energy, and the highest energy $^2\Sigma^+_{1/2}$ state D. (Note that Dabrowski and Herzberg[14] in their analysis of $HeNe^+$ and Dabrowski, Herzberg, and Yoshino[15] in their analysis of $NeAr^+$ label the ground state X and the first two excited states A_1 and A_2, not B $^2\Pi_{3/2}$ and B $^2\Pi_{1/2}$. The notation of Huber and Herzberg[12] for the heavier diatomics also differs from that employed here.)

The photoionization spectrum of X_2 or XY consists of contributions both from direct ionization and from autoionization of Rydberg states of the neutral molecule. Since the Franck-Condon overlap between the ground state of the neutral molecule and the ground state of the ion is poor for several tenths of a volt above the ionization threshold,[11,16] the photoionization spectrum in the region of the ionization threshold consists solely of autoionization structure. At shorter wavelengths, the autoionization structure appears superimposed on the direct ionization continuum. In the present work, we are concerned primarily with the molecular autoionization features and their relationship to the atomic Rydberg states.

For the homonuclear diatomic molecules, the most intense transitions are to states that dissociate to $X^* + X(^1S_0)$, where X^* is an excited atomic state that is connected to the ground state via a dipole-allowed transition. There are five dipole-allowed atomic Rydberg series in X, three of which ($ns[3/2]_1^o$, $nd[1/2]_1^o$, and $nd[3/2]_1^o$) converge to the $^2P_{3/2}^o$ ionic limit, and two of which ($ns'[1/2]_1^o$ and $nd'[3/2]_1^o$) converge to the $^2P_{1/2}^o$ ionic limit. Each of the excited states in these series may combine with a rare gas atom in the ground state to form both an 0_u^+ and a 1_u dipole-allowed molecular state. In addition, there will be a much larger number of weaker 0_u^+ and 1_u molecular Rydberg series resulting from transitions to states that dissociate to $X^*(np, np', nf, nf',\ldots) + X(^1S_0)$ and $X^*(ns, ns', nd, nd')_{J\neq 1} + X(^1S_0)$. Similar considerations apply to the heteronuclear diatomic molecules.

The most significant advantage of photoionization mass spectrometry over photoabsorption for the study of the Rydberg states of the homonuclear and heteronuclear rare gas dimers is the ability of the former technique to discriminate against atomic structure through mass analysis of the product ions. In photoabsorption, the molecular structure is completely masked by the much more intense atomic structure near all of the optically allowed atomic Rydberg transitions.[17] This is not a serious problem near the low lying atomic Rydberg transitions, since the atomic structure is widely spaced; however, in the region between the atomic fine structure thresholds, the atomic structure is not discrete, but, rather, is a true (albeit structured) continuum. Thus it is impossible to observe weak dimer structure superimposed on this very intense atomic continuum in photoabsorption studies.

The obvious and only serious disadvantage of the present technique is the inability to measure these spectra at high wavelength resolution. At present, the best resolution used to study a van der Waals molecule in a photoionization mass spectrometry experiment is 0.07 Å for Ar_2.[4] The spectra reported here were determined at a resolution of 0.07 to 0.45 Å. This resolution frequently is sufficient to resolve much of the structure (indeed, many features are broadened as a result of autoionization and/or predissociation), but higher resolution is necessary to resolve all of the details of various vibrational progressions.

III. EXPERIMENTAL APPARATUS

A photoionization mass spectrometer which incorporates a high intensity VUV light source was used for these studies. The apparatus consists of a helium continuum light source, a GCA/McPherson model 225M16 1 meter near-normal incidence monochromator which disperses and then refocuses the selected light onto the exit slit, a set of ion extraction and focusing lenses, and a differentially pumped quadrupole mass filter for ion detection.

The Hopfield continuum of helium is generated in a 50 cm long capillary lamp by a high voltage pulsed dc discharge. The lamp is operated at a pressure of approximately 100 Torr, with helium admitted at the anode (the end nearest the monochromator entrance slit). The gas flows through the entrance slit into the monochromator; however, an auxiliary pump connected to the cathode maintains a substantial gas flow from anode to cathode, which reduces slit clogging from sputtered material passing through the slits.[18] A Velonex model 350 high power pulse generator is used as the driver for two additional stages of high power pulse amplification. The final output stage is a pair of Machlett 6544 triode tubes in parallel.[19] The photon flux from this lamp at the peak of the helium continuum (820 Å) is approximately 1 x 10^{10} photons/sec/Å.

Figure 3 shows an overview of the ionization region, ion optics, and quadrupole mass filter. In the present experiments, the ionization region is defined by a small gridded cage which is attached to the exit arm of the monochromator. Photoions are repelled out of this cage by a flat repeller plate and are focused onto the entrance aperture of the quadrupole mass filter (Extranuclear model 4-324-9) by the simple stack of focusing and deflection plates. In normal operation, the cage and exit arm of the monochromator are floated at a small positive potential (+15 V) and the rf shield of the quadrupole mass filter is grounded. The use of higher ion injection energies (of up to +100 V) increases the ion collection efficiency, but both the mass resolution and the shape of the mass peak are significantly degraded. Mass selected ions are detected with a channeltron electron multiplier using standard pulse counting techniques. Photons are detected with an aluminum oxide photodiode whose output is measured by a vibrating reed electrometer and subsequently fed into a voltage to frequency converter.

Typical ion backgrounds with either the photon beam flagged or the molecular beam off are a few counts per minute and are due solely to multiplier dark counts, with no contribution from the high voltage pulser. Thus, gating of the ion and photon detectors is unnecessary. The primary source of ion background during an experiment comes from ionization due to scattered light. The scattered light background measured at wavelengths shorter than 580 Å (where there is no light from the helium continuum) is approximately 0.2% of the intensity at the peak of the continuum. This background cannot be gated out by chopping either the photon beam or the molecular beam.

The present experiments use a free supersonic molecular beam source to produce the rare gas dimer species. The molecular beam is parallel to and approximately 1.8 cm from the exit slit of the monochromator, and the jet tip is positioned so that it is as close as possible to the photon beam without intercepting it. The jet is adjustable in three dimensions in order to maximize overlap of the molecular beam with the photon beam. The jet is fabricated by laser microdrilling a hole in a 25 μm thick stainless steel disk, which is then heliarc welded onto the end of a stainless steel tube.

The jet uses no differential pumping and has the advantages of ease of fabrication and the ability to position the tip to within 1 mm of the photon beam, resulting in very high number densities in the ionization region. Typical number densities in a skimmed molecular beam are (1-5) x 10^{12} molecules/cm^3 [(0.3-1.4) x 10^{-4} Torr],[20-22] which is at least two orders of magnitude less than the number densities obtained using the present experimental arrangement. However, the high mass throughput means that with the unskimmed jet the main vacuum chamber operates at high background pressure, occasionally as high as 1 x 10^{-4} Torr. As a result, secondary processes such as associative ionization, collisional ionization, and ion-molecule reactions may occur. In the present experiments, these secondary processes produce no significant interference, and the very large number densities in the ionization region enable high resolution experiments to be performed.

IV. DEPENDENCE OF THE CLUSTER ION SIGNAL ON NOZZLE STAGNATION PRESSURE

The dimer and heavier cluster ion signals depend critically on the combination of nozzle diameter and nozzle stagnation pressure. For example, Figure 4 shows a plot of the pressure dependence of the Ar_n^+ ion signals for n=2–6 measured at a resolution of 0.45 Å. At this wavelength, which is above the $Ar^+\ {}^2P^o_{1/2}$ ionization limit, neither the atom nor any cluster exhibits sharp structure. The ordinate in Figure 4 shows the actual ion counting rate obtained with a 10 μm diameter orifice. Under these conditions the monomer signal increases linearly with stagnation pressure and has a value of 5.5×10^4 counts per second at 2.0 atm. The shapes and relative intensities of the curves in Figure 4 are insensitive to small changes (<20%) in orifice diameter; however, the exact counting rates, especially for the heavier clusters, are very sensitive to the orifice size. A small decrease in orifice diameter uniformly shifts the curves for the heavier clusters to higher stagnation pressures. For a large change in orifice diameter (>50%), the shapes and relative intensities of the curves also are altered. It has been observed in previous studies[23,24] and can be seen in Figure 4 that the dimer can be prepared in the beam over a wide range of pressures where the presence of larger clusters is not detectable. Preparation of a beam containing only monomer, dimer, and trimer is much more difficult, and perhaps impossible, since the tetramer and larger clusters are observed at a stagnation pressure only slightly higher than that at which the trimer is first observed.

There have been several earlier studies on condensation in supersonic beams of Ar using electron impact ionization and varying the nozzle temperature, orifice diameter, and stagnation pressure.[23-27] In a previous electron-impact ionization study,[24] which used large orifices (>100 μm) and a skimmed jet, the dimer ion signal was observed to rise to a maximum, decrease, and then rise again with increasing stagnation pressure. It was postulated that the decrease in dimer signal is due to condensation to form larger clusters, while the second rise is due to fragmentation of larger clusters into dimer. The present photoionization results with an unskimmed jet are consistent with the previous experiments. In all of the results reported here, the nozzle stagnation pressure was adjusted so as to produce a beam that contained primarily monomer and dimer in order to minimize contributions to the dimer ion signal from fragmentation.

V. APPEARANCE POTENTIALS OF THE DIMER IONS AND DISSOCIATION ENERGIES OF THE DIMER ION GROUND STATES

As is shown by Equation (1) below, an accurate value of the adiabatic ionization potential (IP) of a rare gas dimer is required to calculate the dissociation energy (D_0) of the corresponding dimer ion.

$$D_0(XY^+) = IP(Y) + D_0(XY) - IP(XY) \qquad (1)$$

A fundamental problem for the rare gas dimers is that, owing to the large change in geometry that occurs upon ionization, the Franck-Condon factor for ionization to the ground vibrational state is extremely small. For example, the Franck-Condon factor for the argon dimer is negligible for approximately 0.8 eV above the adiabatic ionization potential.[16] Ionization is observed in the threshold region, but is due solely to autoionization. Thus the adiabatic ionization potential will be observed only if there is a high density of autoionizing molecular Rydberg states in the threshold region.

The study of the pressure dependence of the appearance potential of a rare gas dimer helps determine whether the adiabatic ionization potential actually is observed. A comparison of the appearance potential obtained with a low pressure beam (containing only monomer and dimer) and with a high pressure beam (containing a mixture of heavy clusters) is very instructive. A shift of the appearance potential to longer wavelength with increasing nozzle stagnation pressure is evidence that the appearance potential is not the adiabatic ionization potential. No shift of the appearance potential suggests that the adiabatic ionization potential is observed.

Figure 5 shows the Ar_2 threshold region taken at a wavelength resolution of 0.45 Å and at nozzle stagnation pressures of 3.06 and 10.18 atm. In both runs the threshold region shows a weak onset which increases only slowly as a function of excess energy. This gradual rise makes the determination of the appearance potential extremely difficult, and the effects of collisional ionization must be considered carefully. Collisional ionization occurs when neutral dimers are excited to high Rydberg states and gain the energy needed to ionize via collisions. Evidence against significant interference from collisional ionization comes from an examination of the amount of collisional ionization in the photoionization cross section of atomic argon taken under similar experimental conditions. At approximately 1.0 Å below the $Ar^+ \ ^2P^o_{3/2}$ threshold, the intensity of collisional ionization is less than 1% of the intensity of the continuum ionization. Collisional ionization is expected to be even weaker in molecules, since molecular Rydberg states may decay by predissociation which is much faster than any of the competing processes — fluorescence, associative ionization, or collisional ionization. The latter three decay processes are the only ones available to an excited atom. Collisional dissociation of the excited van der Waals molecule also may compete with collisional ionization. Finally, collisional ionization will be structured, reflecting the absorption cross section,[28] not monotonically increasing.

Using the guideline that at 1 Å above the appearance potential the intensity of collisional ionization is 1% of the intensity at the band maximum, and taking into account the effect of instrumental resolution,[29] the appearance potential of Ar_2^+ is determined to be 855.0 ± 1.5 Å for both sets of data shown in Figure 5. Although the threshold region of the high-pressure run rises noticeably more steeply than that of the low-pressure run as a result of fragmentation, the appearance potential does not shift.

The Kr_2^+ threshold is shown in Figure 6 and, like the Ar_2^+ threshold, it does not shift with nozzle stagnation pressure. A sharp step is observed at threshold and there is no evidence of tailing (i.e., of collisional ionization). The steplike behavior of the Kr_2^+ cross section at threshold is qualitatively different from that of Ar_2^+, which shows a gradual onset. The absence of collisional ionization in Kr_2^+ suggests that the tailing in the Ar_2^+ cross section is real and not due to collisional ionization. This of course would shift the Ar_2^+ appearance potential to slightly longer wavelength.

Table I summarizes the best values of the appearance potential of the rare gas dimer ions and the values of the ionization potentials of the free atoms, Table II summarizes the values of the ground state dissociation energies of the neutral molecules, and Table III summarizes the values of the ground state dissociation energies of the ions calculated using Equation (1) and the data from Tables I and II.

Several trends are immediately apparent from the data in Table III. The dissociation energies of the homonuclear dimer ions are much larger than those of the heteronuclear dimer ions. Furthermore the dissociation energy of a heteronuclear dimer ion XY^+ decreases as the mass of Y increases for constant X and as the mass of X decreases for constant Y. These trends can be explained qualitatively using simple molecular orbital theory. Briefly, it can be shown that the bond dissociation energy for a heteronuclear dimer ion is given approximately by[30]

$$D_0 \approx \frac{H_{ab}^{2}}{H_{aa} - H_{bb}} . \qquad (2)$$

Here H_{ij} are the usual Hamiltonian integrals $\int \phi_i H \phi_j dr$, where ϕ_i and ϕ_j are the atomic orbitals and the integration is performed over all space. The denominator of Equation (2) is usually taken to be the difference in ionization potentials of the free atoms. This makes use of Koopmans's theorem[31] which approximates the atomic orbital energy by the ionization potential corresponding to the removal of an electron in that orbital. It is further assumed in Equation (2) that the effect on the atomic energies due to the presence of the other atom is small. Equation (2) predicts that the binding energy increases as the difference in ionization energies of the atomic rare gas partners decreases, which is in agreement with observation in both the rows (constant X) and the columns (constant Y) of Table III.

If one assumes that the charge on a heteronuclear dimer ion resides primarily on one of the atoms, then the rows in Table III are composed of dimers having the same neutral partner throughout and the columns are composed of dimers having the same charged partner throughout. In addition to the effect on the dissociation energy due to the difference in orbital energies of the free atoms, one must also consider the effect due to the change in the polarizability of the neutral partner. A further effect, although one which is sometimes difficult to observe due to stronger competing effects, results from the change in R_e throughout the rows and columns.

For systems in which the chemical effects are small, a substantial part of the binding should be due to the ion-induced dipole interaction, which is given by $-\alpha e^2/2R^4$, where α is the atomic polarizability. In the sequence $NeXe^+$, $ArXe^+$, $KrXe^+$, the increase in the ion-induced dipole energy from $NeXe^+$ to $KrXe^+$ due to the increase in polarizability is more than a factor of 6,[32] while the decrease in the ion-induced dipole energy due to the increase in R_e is only about a factor of 2.[33] We conclude that the increase in dissociation energy in going from $NeXe^+$ to $KrXe^+$ or from $NeKr^+$ to $ArKr^+$ is due to increased polarizability of the neutral partner as well as to increased chemical effects predicted by the difference in orbital energies of the free atoms.

The numerator in Equation (2), which is the "interaction energy," is often assumed to be proportional to the overlap integral $S_{ab}(\equiv \int\phi_a\phi_b dr)$[34] and the overlap is expected to increase as R_e decreases, which is in agreement with the observed trend in the rows and is the same as the trend predicted by the difference in ionization potentials of the free atoms. In the columns, even though R_e decreases in going from $KrXe^+$ to $NeXe^+$, the dissociation energy decreases due to the overwhelming effects of the increased difference in orbital energies of the free atoms and the rapid decrease in polarizability of the neutral partner.

The dissociation energies of the ground states of the homonuclear dimer ions follow the same trend that is observed for the heteronuclear rare gas dimer ions, i.e., $D_0(Ar_2^+) > D_0(Kr_2^+) > D_0(Xe_2^+)$; however, the explanation is more complicated. The decrease in dissociation energy in going from Ar_2^+ to Xe_2^+ depends on a number of factors and is ultimately the result of spin-orbit interaction. Recent calculations[10] show that, in the absence of spin-orbit coupling, the dissociation energies show only a very slight decrease with increasing reduced mass.

VI. MOLECULAR RYDBERG STRUCTURE BETWEEN THE ATOMIC FINE-STRUCTURE THRESHOLDS and DISSOCIATION ENERGIES OF X_2^+ C $^2\Pi_{1/2u}$ and XY^+ B $^2\Pi_{1/2}$ and D $^2\Sigma^+_{1/2}$

The molecular spectra of the homonuclear and heteronuclear rare gas dimers show strong similarities to the corresponding atomic structure in the energy region between the atomic $^2P^o_{3/2}$ and $^2P^o_{1/2}$ fine-structure thresholds. In the homonuclear dimers, molecular Rydberg series are observed that converge to the C $^2\Pi_{1/2u}$ and D $^2\Sigma^+_{1/2g}$ states of the dimer ion (see Figure 1); however, the D $^2\Sigma^+_{1/2g}$ state is either very weakly bound or purely repulsive and molecular Rydberg states converging to it are not seen in photoionization. In the heteronuclear dimers, the molecular Rydberg series converge to either the B $^2\Pi_{1/2}$ or D $^2\Sigma^+_{1/2}$ state of the ion, depending on whether the energy region corresponds to the region between the Y^+ or the X^+ fine-structure thresholds (see Figure 2). This is a particularly simple region of the spectrum for most of the heteronuclear rare gas dimers, since all of the molecular Rydberg states converge to a single ionic limit. In addition, much of the molecular structure retains the characteristic Beutler-Fano profiles observed in the atomic spectra.

Figures 7 to 9 summarize the results in the following format. The uppermost plot in each figure shows the atomic spectrum in the region between the $^2P^o_{3/2}$ and $^2P^o_{1/2}$ fine-structure thresholds. Figures 7, 8, and 9 present the results for Ar, Kr, and Xe, respectively. The additional plots in each figure show the homonuclear and heteronuclear dimer spectra in the same energy region as the corresponding atomic spectrum. (Note that, in each of the figures, one of the heteronuclear dimer spectra is missing, either because it is too weak to be observed on the direct ionization background or because it is masked by Rydberg structure associated with other series.) Figure 9 shows the spectra of Xe, NeXe, ArXe, and Xe_2 and is a striking example of the progression from a spectrum that shows a strong resemblance to the atomic spectrum (NeXe) to a spectrum that shows only modest resemblance to the atomic spectrum (Xe_2). Similar results are obtained for the Ar series (Figure 7) and the Kr series (Figure 8).

The effective principle quantum number n^* of each molecular state was calculated using the relation

$$n^* = [Ry/(E_\infty - E_{obs})]^{1/2} \tag{3}$$

where Ry is the Rydberg constant, E_{obs} is the observed excitation energy, and E_∞ is the vertical ionization potential of the ionic convergence limit. In all cases, the peak positions were taken to be the band maxima. Because of the pronounced Beutler-Fano profiles in some of the bands, the band maxima can be red shifted from their respective centerlines. Care was taken to choose the atomic and molecular peak postions in a consistent manner. For the homonuclear dimers, the vertical ionization potential of the C $^2\Pi_{1/2u}$ state, which is obtained from the high resolution photoelectron spectra,[11,16] is used as the series limit. Since no photoelectron spectra have been reported for the heteronuclear dimers, an initial estimate of the vertical ionization potential of the ionic convergence limit was obtained by shifting the atomic ionization potential by the amount that the molecular peaks are shifted from the corresponding atomic peaks. The value of E_∞ was varied until the most nearly constant set of values for the non-integral part of n^* was obtained, and the final value of E_∞ was taken to be the vertical ionization potential of the ionic state. Since there is only one ionic state to which these series may converge, the ns′ and nd′ series must both be fit by the same value of E_∞.

The dissociation energy of a given Rydberg state is given by

$$D_0(XY^*) = E(X^* \text{ or } Y^*) + D_0(XY) - E_{obs}(XY^*) + \Delta \qquad (4)$$

where $E(X^*$ or $Y^*)$ is the excitation energy of the atomic Rydberg state to which XY^* dissociates, $D_0(XY)$ is the dissociation energy of the neutral ground state, and Δ is the difference in energy between the vertical and adiabatic excitation energies, i.e., the difference in energy between the transition to the maximum of the Franck-Condon envelope and the transition to the $v' = 0$ level of the Rydberg state. Because the potential energy curves of the highly excited Rydberg states are similar to the potential energy curve of the ionic convergence limit, Δ was estimated for the homonuclear dimers to be the difference in the vertical and adiabatic ionization potentials, with both quantities obtained from the photoelectron spectrum. No values of the adiabatic ionization potentials exist for the B $^2\Pi_{1/2}$ and D $^2\Sigma^+_{1/2}$ states of heteronuclear dimers, and thus only values of the quantity $(D_0 - \Delta)$ are reported. For both the homonuclear[11,16] and the heteronuclear dimers, Δ is expected to be a small fraction of the dissociation energy.

Tables IV and V give representative results for a homonuclear diatomic molecule (Ar_2) and a heteronuclear diatomic molecule (ArXe), respectively. Included in these tables are the molecular peak positions in angstroms and eV, and the value of n^* calculated from Equation (3). Also given are the energetics of the assumed dissociation limit, including the value of n^* for the atomic transition corresponding to the dissociation limit, and the values of $(D_0 - \Delta)$ for each assigned molecular transition and for the series limit (i.e., the ionic state). Table VI summarizes the values of D_0 and $(D_0 - \Delta)$ for the excited states of all of the rare gas dimers and includes values determined from a variety of spectroscopic and molecular beam scattering measurements.

At large internuclear separation, the potentials of the excited states of the rare gas dimers are described by dispersion forces, with the dominant contribution arising from the ion-induced dipole term given by $-\alpha e^2/2R^4$, where α is the atomic polarizability. This potential has been evaluated at the equilibrium internuclear separation of each neutral rare gas dimer, and the results are compared with experiment in Table VII. For the homonuclear dimers, the agreement is fair for Ar_2, but becomes progressively worse for Kr_2 and Xe_2. This is best understood by remembering that spin-orbit coupling mixes the A $^2\Sigma^+_{1/2u}$ and C $^2\Pi_{1/2u}$ ionic states.[1] This mixing increases from Ar_2 to Xe_2, and results in a decrease in dissociation energy of the relatively strongly bound A $^2\Sigma^+_{1/2u}$ state, with a concurrent increase in dissociation energy of the C $^2\Pi_{1/2u}$ state. The increase in binding energy of the C $^2\Pi_{1/2u}$ state is considerably greater than that predicted by the ion-induced dipole potential. Hence, while the ion-induced dipole potential appears to be a reasonable approximation for the C $^2\Pi_{1/2u}$ state of Ar_2^+ and the Rydberg states converging to it (at $R = R_e$ of Ar_2), the increased binding in Kr_2 and Xe_2 due to spin-orbit mixing makes the ion-induced dipole potential a poor approximation for these molecules. The agreement is considerably better for the heteronuclear dimers, especially for those containing Ne; however, in general, this approximation is not expected to be a good one at the internuclear distance corresponding to R_e of the ground state. This may be true even for weakly bound van der Waals molecules, for which R_e can be quite large.

VII. MOLECULAR RYDBERG STRUCTURE IN THE SPECTRA OF NeY NEAR THE Ne 3s ATOMIC RESONANCE

In principle, the energy region near the lowest lying Rydberg state (i.e., the resonance transition) of a rare gas atom will provide the best opportunity for studying molecular states that are well separated from adjacent levels. The resonance levels of the rare gas atoms are below the ionization potential of the homonuclear dimers, and therefore molecular states arising from these dissociation limits cannot be observed in photoionization mass spectrometry; however, this is not the case for the heteronuclear Ne-rare gas dimers. The Ne^*3s resonance levels are above the molecular ionization potential of these dimers and therefore molecular states in this energy region can be studied using photoionization techniques. Only five dipole-allowed molecular Rydberg states arise from the combination of a rare gas atom in the $^1S_0$ ground state and a neon atom in one of the four atomic states arising from the configuration $1s^22s^22p^53s$, i.e., $3s[3/2]^o_1$, $3s[3/2]^o_2$, $3s'[1/2]^o_1$, and $3s'[1/2]^o_0$. The atomic states with $J=1$ are the familiar dipole-allowed neon resonance lines and those with $J=0$ or 2 are the dipole-forbidden (metastable) states employed in neon scattering experiments.

Figure 10 shows the relative photoionization cross sections of NeAr, NeKr, and NeXe in the wavelength region from 730 to 750 Å. The same NeAr spectrum, together with the NeAr spectrum obtained using an effusive rather than a supersonic molecular beam source, is shown in Figure 11. The four atomic states derived from the excited state neon configuration $1s^22s^22p^53s$ are[35] $3s[3/2]^o_2$ at 746.025 Å, $3s[3/2]^o_1$ at 743.7195 Å, $3s'[1/2]^o_0$ at 741.726 Å, and $3s'[1/2]^o_1$ at

735.8962 Å. There are no other excited states of Ne or of Ar, Kr, or Xe in this wavelength region.

All three molecular spectra show both a narrow band at approximately the position of the $3s'[1/2]_1^o$ transition and a broader band blue shifted from this level. The position of the dip between the two bands occurs at the energy of the molecular dissociation limit (which is blue shifted from the position of the $Ne^*3s'[1/2]_1^o$ transition by an amount equal to the dissociation energy of the NeY ground state). The narrower feature is attributed to a transition to bound levels of a molecular state dissociating to $Ne^*(3s'[1/2]_1^o) + Y(^1S_0)$. The band is characterized by a sharp onset that is red shifted from the position of the resonance transition and a width that is broader than the spectrometer resolution. Both the width of the peak and the magnitude of the red shift increase from NeAr to NeXe and give an indication of the binding in this state. As the pressure in the ionization region is increased, the relative intensity of the narrow band decreases slightly with respect to that of the broad band.

The broad peak which is blue shifted from the $Ne^*3s'[1/2]_1^o$ atomic resonance position in all three neon-rare gas dimer spectra also is attributed to a transition to a molecular state dissociating to $Ne^*(3s'[1/2]_1^o) + Y(^1S_0)$. This peak results from excitation to the repulsive wall of the NeY^* potential curve, followed by electronic autoionization to give $NeY^+ + e$. This process can be likened to an associative ionization half-reaction in which, at a given wavelength, the NeY^* collision complex is prepared with a fixed relative translational energy determined by the position of excitation on the repulsive wall. Because the rotational energy of the NeY dimer is not altered significantly by the absorption of a photon, the collision complex is formed with approximately thermal (20 K) rotational energy, which corresponds to a relatively small impact parameter collision.

If one assumes that the molecular absorption oscillator strengths for transitions to states dissociating to $Ne^*(3s[3/2]_1^o$ or $3s'[1/2]_1^o) + Y(^1S_0)$ are proportional to the corresponding atomic oscillator strengths, then molecular structure should be observed in the NeY photoionization cross sections near the $3s[3/2]_1^o$ level and should be approximately a factor of 15 weaker than the structure near the $3s'[1/2]_1^o$ level.[36] An examination of the data shown in Figure 10 reveals a weak broad peak in the NeAr spectrum to the blue of the $3s[3/2]_1^o$ transition with a width approximately equal to that of the molecular peak near the $3s'[1/2]_1^o$ transition. No similar features were observed in the NeKr or the NeXe spectra, but small variations in transition probability, Franck-Condon factors, or autoionization efficiency could make them undetectable. No structure is observed in any of the spectra near the neon metastable states, as is expected from the forbidden nature of these atomic transitions.

The NeKr and NeXe associative ionization spectra obtained with a effusive molecular beam source are similar to the spectrum shown in Figure 11 for NeAr. The background pressure in the ionization chamber during the effusive beam experiments was identical to that during the corresponding supersonic beam experiments; thus, the intensity of the associative ionization structure should be similar in both spectra. In all cases, the intensity of the associative ionization peak at the position of the $Ne^*3s[3/2]_1^o$ resonance transition was nearly equal to the intensity of the corresponding peak in the spectrum obtained using a supersonic molecular beam source, suggesting that this structure is due in large part to associative ionization. Since associative ionization is about a factor of 4 weaker for the $3s'[1/2]_1^o$ state than for the $3s[3/2]_1^o$ state, it contributes negligibly to the molecular structure observed near the $3s'[1/2]_1^o$ transitions in the spectra taken with the supersonic molecular beam source.

The two features observed in the Ne-rare gas photoionization spectra near the $Ne^*3s'[1/2]_1^o$ resonance line must result from transitions to one or possibly both of the dipole-allowed molecular states arising from the $Ne^*(3s'[1/2]_1^o) + Y(^1S_0)$ dissociation limit. These states have 0^+ and 1 symmetry. It is possible to hypothesize a mechanism to explain the observed biomodal spectral structure that involves transitions to a single excited state. According to this hypothesis, a single state of the Ne^*-rare gas excimer is populated in photoabsorption. It is well known that the absorption cross section must be continuous at the dissociation limit.[37] We postulate that the dip in the photoionization cross section at the dissociation limit results from the difference in decay rates between the bound and continuum vibrational levels. The bound levels may decay via fluorescence, autoionization, or predissociation; the continuum levels may decay via direct dissociation as well as the above mechanisms, and direct dissociation is expected to rapidly depopulate the molecular states. Thus, the ionization cross section may well show a discontinuity at the dissociation limit, with that part of the cross section corresponding to transitions to bound vibrational levels being relatively more intense. This is indeed what is observed. The pressure dependence of the cross section also is consistent with this mechanism; namely, the long-lived bound vibrational levels are more pressure sensitive than the short-lived continuum levels.

We have performed calculations to determine whether the shape of the photoionization cross section above the molecular dissociation limit can be reproduced using the potential energy curves obtained from scattering data. The calculations assume that the energy dependence of the absorption cross section is proportional to the Franck-Condon factor and that the autoionization rate is proportional to the associative ionization cross section at the appropriate relative translational energy.[38] This further assumes that the electronic matrix element is invariant with energy and that the interaction between the autoionizing state and the direct ionization continuum does not affect the line shape of the discrete state (i.e., the Fano q parameter is large).[39]

For each Ne-rare gas system, the ground state potential energy curve was taken from the work of Ng et al.[40] and the upper state NeY^* potential energy curve was the IAMMSV (ion-atom Morse-Morse spline van der Waals) potential determined by Gregor and Siska.[41] Figure 12 shows an example of these potential energy curves for NeAr. The vibrational temperature of the dimers formed in the expansion was assumed to be 20 K; however, this value is not known accurately and the effect of varying it was examined.

The Franck-Condon factors were determined using the delta function approximation,[42] which has been employed in a number of calculations involving bound-free transitions. In this approximation, the upper state continuum wave function is set equal to a delta function at the classical turning point and the Franck-Condon distribution is obtained by reflecting the square of the ground state wave function off of the upper state potential curve. Briefly, the steps in the calculation were as follows:

(1) The ground state vibrational wave functions $\psi_i(R)$ were calculated for each initial vibrational level i.

(2) The absorption cross section for each vibrational level (i.e., the Franck-Condon distribution) was determined by reflecting $\psi_i^2(R)$ from the upper state potential energy curve to give $\psi_i^2(\Delta E)$, where ΔE is the transition energy.

(3) The weighted cross sections were calculated by multiplying the cross section for each vibrational level by the appropriate Boltzman factor f_i at 20 K to give $f_i \psi_i^2(\Delta E)$.

(4) The relative photoionization cross section for a given initial vibrational level was calculated by multiplying each weighted cross section by the (energy dependent) associative ionization cross section to give $\sigma_{AI}(\Delta E) f_i \psi_i^2(\Delta E)$.

(5) The total photoionization cross section was calculated by summing the contributions from the individual vibrational levels.

The relative ionization cross section was then normalized to the experimental data by equating the maxima of the theoretical and experimental distributions. Because the experimental associative ionization cross sections are limited to translational energies greater than 0.01 eV, the calculated cross sections start slightly to the blue of the position of the $\mathrm{Ne}^* 3s'[1/2]_1^o$ transition.

The results are shown in Figure 13. The agreement with experiment is very good for NeXe, but the width of the theoretical distribution is smaller than that of the experimental distribution for both NeKr and NeAr. Increasing the assumed temperature of the beam increases the width of the theoretical distribution only slightly, as the dominant effect of a higher temperature is to increase the contributions of large R values in the calculation of the Franck-Condon factor, which leads to transitions to the bound portion of the excited state.

The shape of the theoretical distribution is extremely sensitive to the slope of the repulsive wall of the excited state; increasing this slope dramatically improves the fit to the NeAr data. We expect that this simple model can be improved and extended by more accurate theoretical work and, together with data from scattering experiments, may lead to more accurate potentials for these neon-rare gas excimers.

VIII. MOLECULAR RYDBERG STRUCTURE IN THE SPECTRA OF ArKr AND ArXe NEAR THE Ar 5s AND 3d ATOMIC RESONANCES

The energy region near the first resonance transition in Ar (the 4s levels) is not accessible in photoionization since it is energetically below the ionization thresholds of ArKr and ArXe; however, the energy region near the second transiton in Ar does lie above the ionization thresholds of these heteronuclear dimers. Unfortunately the atomic Ar 5s energy levels are nearly degenerate with the 3d levels, and the photoionization cross sections for ArKr and ArXe near these atomic levels are expected to be much more complex than those observed for the heteronuclear dimers containing Ne near the Ne 3s levels.

Figure 14 shows the relative photoionization cross sections for ArKr and ArXe between 860 and 890 Å determined at a wavelength resolution of 0.28 Å. Going to still higher resolution (0.15 Å) resolves no new features, indicating that the spectral features are broadened by autoionization and/or predissociation. This wavelength region contains five dipole allowed states of atomic Ar based on the 5s and 3d configurations. These states are indicated in Figure 14. Autoionizing molecular states of 0^+ and 1 symmetry derived from the combination $Ar^*(5s \text{ or } 3d)_{J=1}$ + $Xe(^1S_0)$ are expected to account for much of the prominent structure in the ArXe spectrum. The situation is more complex for ArKr owing to the presence of the atomic Kr^*(ns′ and nd′) Rydberg levels; however, the strong similarity of the ArKr and ArXe spectra in this wavelength region indicates that the molecular states dissociating to Ar^*(5s or 3d) + Kr ($^1S_0$) dominate the ArKr spectrum. This is in accord with the fact that the atomic transition probabilities are greater to the low lying states of Ar than to the higher lying states of Kr.

There is a very approximate correlation of the structure in ArKr and ArXe spectra, with the structure in the ArXe spectrum red-shifted by 1-2 Å from the corresponding structure in the ArKr spectrum. The detailed correlation with the atomic Ar spectrum is not obvious and the spectra are clearly more complex than the simple red- or blue-shifted bands observed in the heteronuclear dimers containing Ne. It is possible, as was suggested by Ng et al.,[43] that the bands that are blue shifted from the dipole-allowed atomic Ar levels result from transitions to molecular states with potential humps. However, at least two other explanations may also account for these features. First, as in the case of the Ne-rare gas dimers, the blue-shifted bands may result from excitation to the repulsive wall of ArY^* followed by rapid autoionization to form ArY^+. Second, the bands may result from transitions to molecular states that dissociate to one of the many dipole-forbidden atomic Ar levels that are in this wavelength region. It is doubtful that these spectra will be understood completely without the help of theoretical calculations.

IX. MOLECULAR RYDBERG STRUCTURE IN THE SPECTRA OF X_2 AND XY NEAR THE HIGH-LYING ATOMIC RYDBERG STATES

The structure in the molecular spectra near the high-lying atomic Rydberg states is extremely complex and is only partially amenable to analysis. For example, the spectra of Ar_2, ArKr, and ArXe determined at a resolution of 0.15 Å in the region 800 to 850 Å are shown in Figures 15a and 15b. The features in the photoionization cross sections of ArKr and ArXe in this wavelength region result from transitions to states that dissociate to Ar^*(ns or nd) + $Y(^1S_0)$, where n>6 for s states and n>4 for d states. The atomic Ar Rydberg series are indicated in the figures, and it is immediately obvious that there is little correlation between the atomic and the molecular Rydberg series in this wavelength region. (It should be remembered that the weak, sharp peaks occuring at the exact postions of the atomic Ar transitions are due to the associative ionization reaction $Ar^* + Y \rightarrow ArY^+ + e$).

There is a similarity in the spectra of ArKr and ArXe, although the ArXe bands are red-shifted by approximately 1-1/2 to 2 Å from the corresponding bands in ArKr, and they show more discrete structure than do the ArKr bands. The correlation of features in ArKr and ArXe with those in Ar_2 is less obvious. This probably results from the differences in the molecular ion convergence limits for the homonuclear and heteronuclear dimers and the consequent differences in the Rydberg structure.

In general, a detailed analysis of the bands is not possible using spectra obtained at 0.15 Å resolution. We have determined the energy spacings for all peaks within (what appear to be) the various vibrational progressions, but the energy differences are erratic and there is considerable overlapping of bands. The fact that excitation occurs at relatively large internuclear distance corresponding to R_e of the neutral dimers may be partially responsible for the complicated spectra. Vertical transitions are made to states in a region where configuration mixing is often extremely important,[44] and can lead to complicated potential energy curves.

Many of these bands have vibrational structure with spacings of 50-70 cm^{-1}, which is consistent with the magnitudes of the dissociation energies of the excited states of the ions reported in Table VI. Using this observation, we have performed a simple analysis of the regularly spaced features in the Ar_2 spectrum in the wavelength region from 822 to 826 Å. The prominent peaks are listed in Table VIII along with assignments and energy differences. The energy spacings between peaks are similar to the vibrational spacings in the B $^2\Pi_{3/2g}$ state of the ion, suggesting that this structure corresponds to vibrational members of a Rydberg state converging to this limit. In order to quantify this comparison, the Franck-Condon factors were calculated for the X $^1\Sigma_g^+$, $v'' = 0$ $\rightarrow$ B $^2\Pi_{3/2g}$, v' ionizing transition. For this calculation, a Morse potential was used for the X $^1\Sigma_g^+$ ground state, with $R_e = 3.76$ Å, $\omega_e = 30.68$ cm^{-1}, and $D_e = 98.70$ cm^{-1}.[4] A numerical potential was used for the B $^2\Pi_{3/2g}$ state and was based on the shape of the curve calculated by Wadt,[10] but was scaled to give the experimental dissociation energy of 0.14 eV.[16] The vibrational energy levels, values of $\Delta G_{v' + 1/2}$, and Franck-Condon factors from X $^1\Sigma_g^+$, $v'' = 0$ are given in Table IX. Near the maximum in the Franck-Condon distribution, the values of $\Delta G_{v' + 1/2}$ range from 65 to 100 cm^{-1} and encompass seven vibrational levels, which is in reasonable agreement with the observations. The most probable dissociation limit for this state is the $5d[1/2]_1^o$ atomic level.

Part of the reason for the complexity of these spectra may be seen by considering the spectrum of Ar_2 in the wavelength region from 836 to 842 Å. The structure in this region is red shifted by several angstroms from the $6s[3/2]_1^o$ atomic transition. It is of interest compare the molecular structure in this region with that near the $4s[3/2]_1^o$ resonance at 1066.66 Å and the $5s[3/2]_1^o$ resonance at 879.95 Å.[35] A strong band system containing 30 bands appears in the region 1065-1073 Å (Tanaka and Yoshino Band System II)[17] and transitions are observed to seven vibrational levels of the upper state with $\Delta G_{v'} + 1/2$ values ranging from 78 to 137 cm^{-1}. A similar, although weaker, band system appears in the region 884-892 Å (Tanaka and Yoshino Band System VIII)[17] and shows long v′ progressions with individual bands degraded toward short wavelengths. The $\Delta G_{v'} + 1/2$ values range from 60 to 128 cm^{-1}. The structure in the wavelength region to the red of the $6s[3/2]_1^o$ atomic transition is significantly different from that just described for the $4s[3/2]_1^o$ and $5s[3/2]_1^o$ atomic transitions. Figure 15b shows that, in the photoionization spectrum, no regular extended vibrational progression is observed. (The absorption and ionization spectra are very similar throughout most of this region; in other words, the photoionization spectrum does not discriminate against absorption features that predissociate.) Thus, the molecular Rydberg states in the region near the $6s[3/2]_1^o$ atomic resonance must be significantly different from their counterparts at longer wavelength. One obvious complication is that the atomic $6s[3/2]_1^o$ and $4d[3/2]_1^o$ energy levels are nearly coincident and, as a result, the molecular states arising from these dissociation limits will be subject to mutual perturbations. Moreover, in addition to these two dipole-allowed energy levels, there exist a large number of dipole-forbidden atomic energy levels which can combine with a ground state argon atom to form an 0_u^+ and 1_u molecular state. While transitions to these molecular states are expected to be weaker than those to states dissociating to a J=1 atomic level, they will undoubtedly complicate the spectrum through perturbations and avoided crossings.

Figure 16 shows the data in this region taken at a resolution of 0.07 Å. All of the possible atomic dissociation limits are shown, with the optically allowed atomic energy levels indicatd by heavy lines. The 0_u^+ and 1_u molecular states arising from the combination of the excited state atom with a ground state atom are also shown. The atomic transitions are shifted in energy by an amount equal to $D_0(Ar_2)$, which places the atomic and molecular transitions on the same energy scale assuming that all of the molecular transitions originate in $v'' = 0$ of the ground state. There are 15 0_u^+ and 1_u molecular states in the energy region shown in Figure 16, resulting in a very large number of possible interactions. It is thus not surprising that few regularities are observed in the spectrum.

A second example of the complexity of the dimer spectra is shown in the region from 925 to 940 Å in the spectrum of the heteronuclear dimer KrXe. This region, which is shown in Figure 17, shows a long series of weak peaks superimposed on the direct ionization continuum. The wavelength positions and energy separations between peaks are given in Table X. This region contains the convergence limit of the molecular Rydberg series that dissociate to $Kr(^1S_0)$ + Xe(ns′ or nd′). The analogous series in ArXe converge to a limit at 925.90 Å and those in Xe_2 converge to a limit at 931.24 Å. However, the spacings of the observed peaks in KrXe do not indicate a converging series and it is therefore more likely that these peaks are part of a vibrational progression associated with a state that dissociates to Kr^* + $Xe(^1S_0)$. The most likely candidates for the Kr^* state are the $8s[3/2]_1^o$ level at 922.73 Å and $6d[3/2]_1^o$ at 923.71 Å;[35]

however, the spacings of the peaks listed in Table X are irregular and no reasonable Birge-Sponer plot results. The origin of the intense peak at 928.5 Å is not known, but it is possible that the weaker peaks gain sufficient intensity to be observed through interaction with this state.

X. SUMMARY AND CONCLUSIONS

We have described the photoionization cross sections for homonuclear and the heteronuclear dimers in the wavelength region from the molecular ionization potential to the ${}^2P^o_{1/2}$ ionization limit of the lighter atom. In the spectral region between the atomic fine-structure thresholds, a simple analysis based on the value of the effective principal quantum numbers n^* and on the observed similarity between the atomic and molecular structure shows that most of the structure can be readily interpreted in terms of Rydberg series converging to an excited state of the ion. Vertical binding energies are obtained for both the Rydberg states and the ionic convergence limits.

In comparing the atomic and molecular spectra in the region between the atomic fine-structure thresholds, one cannot help but note the striking similarity among them, and it is tempting to generalize this observation and conclude that molecular spectra of van der Waals molecules are merely weakly perturbed atomic spectra. However, there are significant differences in the atomic and molecular spectra in regions other than that between the atomic fine-structure thresholds. Long vibrational progressions are observed in the spectra determined at a resolution of 0.15 Å, indicating that it is an oversimplification to characterize the molecular spectra as perturbed atomic spectra.

Ginter et al.[45] have cautioned against the use of low resolution spectra (i.e. rotationally unresolved) such as those presented here for the determination of structural assignments, since the probability of guessing a correct solution is very low using an analysis based solely on quantum defects. We have found that higher resolution data certainly would be necessary to analyze the complex vibrational progressions observed in Ar_2, ArKr and ArXe between 800 and 850 Å (Figures 15a and 15b). In the region of the Beutler-Fano profiles, the quantum defect analysis is more reliable, however, because of the additional information contained in the lineshapes of the bands. This rather fortunate situation allows the determination of the (vertical) dissociation energies of the Rydberg states and of the excited state of the ions, quantities which cannot be obtained from a conventional absorption spectrum. Furthermore, the adiabatic ionization potential (and hence the dissociation energy of the ground state of the ion) can be determined from the present experiments, but not from the absorption spectrum, since the molecular Rydberg series converging to the ionization limit have not been analyzed.

The present data thus serve as an effective complement to absorption spectra obtained using high resolution instruments (i.e. those having resolving powers greater than 100,000), and the technique of photoionization mass spectrometry is shown to be a useful method for obtaining certain spectral and thermodynamic information on van der Waals molecules that is not readily obtainable using conventional absorption spectroscopy.

REFERENCES

1. R. S. Mulliken, J. Chem. Phys. 52, 5170 (1970).
2. D. S. Ginter and M. L. Ginter, J. Mol. Spectrosc. 82, 152 (1980) and references therein.
3. P. M. Dehmer and E. D. Poliakoff, Chem. Phys. Lett. 77, 326 (1981).
4. P. M. Dehmer, J. Chem. Phys. 76, 1263 (1982).
5. S. T. Pratt and P. M. Dehmer, Chem. Phys. Lett. 87, 533 (1982).
6. P. M. Dehmer and S. T. Pratt, J. Chem. Phys. 75, 5265 (1981).
7. S. T. Pratt and P. M. Dehmer, J. Chem. Phys. 76, 3433 (1982).
8. P. M. Dehmer and S. T. Pratt, J. Chem. Phys. (submitted).
9. D. J. Trevor, Ph.D. thesis, University of California, Berkeley, 1980.
10. W. R. Wadt, J. Chem. Phys. 68, 402 (1978).
11. P. M. Dehmer and J. L. Dehmer, J. Chem. Phys. 68, 3462 (1978).
12. K. P. Huber and G. Herzberg, Molecular Spectra and Molecular Structure IV. Constants of Diatomic Molecules (Van Nostrand Reinhold Company, New York, 1979).
13. C. F. Bender and N. W. Winter, Appl. Phys. Lett. 33, 29 (1978).
14. I. Dabrowski and G. Herzberg, J. Mol. Spectrosc. 73, 183 (1978).
15. I. Dabrowski, G. Herzberg, and K. Yoshino, J. Mol. Spectrosc. 89, 491 (1981).
16. P. M. Dehmer and J. L. Dehmer, J. Chem. Phys. 69, 125 (1978).
17. See for example Y. Tanaka and K. Yoshino, J. Chem. Phys. 53,, 2012 (1970).
18. W. A. Chupka and J. Berkowitz, J. Chem. Phys. 51, 4244 (1969).
19. W. A. Chupka, P. M. Dehmer, and W. T. Jivery, J. Chem. Phys. 63, 3929 (1975).
20. C. Y. Ng, D. J. Trevor, B.H. Mahan, and Y. T. Lee, J. Chem. Phys. 66, 446 (1977).

21. W. M. Trott, N. C. Blais, and E. A. Walters, J. Chem. Phys. 69, 3150 (1978).

22. Y. Ono, S. H. Linn, H. F. Prest, M. E. Gress, and C. Y. Ng, J.Chem. Phys. 73, 2523 (1980).

23. A. van Deursen, A. van Lumig, and J. Reuss, Int. J. Mass Spectrom. Ion Phys. 18, 129 (1975).

24. (a) D. Golomb, R. E. Good, and R. F. Brown, J. Chem. Phys. 52, 1545 (1970); (b) D. Golomb, R. E. Good, A. B. Bailey, M. R. Busby, and R. Dawbarn, J. Chem. Phys. 57, 3844 (1972).

25. (a) T. A. Milne and F. T. Greene, J. Chem. Phys. 47, 4095 (1967); (b) T. A. Milne, A. E. Vandergrift, and F. T. Greene, J. Chem. Phys. 52, 1552 (1970).

26. R. E. Leckenby, E. J. Robbins, and P. A. Trevalios, Proc. R. Soc. (London) Ser. A 280, 409 (1964).

27. N. Lee and J. B. Fenn, Rev. Sci. Instrum. 49, 1269 (1978).

28. K. Radler and J. Berkowitz, J. Chem. Phys. 70, 221 (1979).

29. P. M. Guyon and J. Berkowitz, J. Chem. Phys. 54, 1814 (1971).

30. J. N. Murrell, S. F. A. Kettle, and J. M. Tedder, The Chemical Bond (Wiley, New York, 1978), pp 82-85, 91, 168.

31. J. H. D. Eland, Photoelectron Spectroscopy (Butterworth, London, 1974).

32. A. Dalgarno and A. E. Kingston, Proc. Roy. Soc. (London) A259, 424 (1961).

33. This assumes that $R_e(XXe^+) \approx 1/2\ R_e(X_2) + [R_e(Xe_2^+) - 1/2\ R_e(Xe_2)]$. While this is admittedly a very rough approximately, it does permit an estimate of the ratio of R_e^4.

34. M. Wolfsberg and L. Helmholz, J. Chem. Phys. 20, 837 (1952).

35. C. E. Moore, Natl. Bur. Stand. Circ. 467, Vol. III (1949).

36. W. L. Wiese, M. W. Smith, and B. M. Glennon, Atomic Transition Probabilities, Vol I, Natl. Stand. Ref. Data Ser., Natl. Bur. Stand. 4, 1966.

37. (a) A. C. Allison and A. Dalgarno, J. Chem. Phys. 55, 4342 (1971); (b) A. L. Smith, J. Chem. Phys. 55, 4344 (1971).

38. (a) R. H. Neynaber and G. D. Magnusen, Phys. Rev. A 11, 865 (1975); (b) R. H. Neynaber and G. D. Magnusen, Phys. Rev. A. 14, 961 (1976); (c) R. H. Neynaber and S. Y. Tang, J. Chem. Phys. 70, 4272 (1979).

39. (a) U. Fano, Phys. Rev. 124, 1866 (1961); (b) U. Fano and J. W. Cooper, Phys Rev. 137A, 1364 (1965).

40. C. Y. Ng, Y. T. Lee, and J. A. Barker, J. Chem. Phys. 61, 1996 (1974).

41. R. W. Gregor and P. E. Siska, J. Chem. Phys. 74, 1078 (1981).

42. G. Herzberg, Molecular Spectra and Molecular Structure I. Spectra of Diatomic Molecules (Van Nostrand, Princeton, 1950), pp 393-394.

43. C. Y. Ng, P. W. Tiedemann, B. H. Mahan, and Y. T. Lee, J. Chem. Phys. 66, 5737 (1977).

44. R. S. Mulliken, J. Am. Chem. Soc. 88, 1849 (1966).

45. M. L. Ginter, D. S. Ginter, and C. M. Brown, Appl. Opt. 19, 4015 (1980).

Table I. Ionization Potentials of the Rare Gas Dimers (eV)

	He	Ne	Ar	Kr	Xe
He					
Ne		20.21 ± 0.05[a]	15.685 ± 0.004[b]	13.950 ± 0.003[b]	12.094 ± 0.004[b]
Ar			14.50 ± 0.03[c]	13.484 ± 0.015[d]	11.968 ± 0.012[d]
Kr				12.866 ± 0.003[e]	11.763 ± 0.011[d]
Xe					11.127 ± 0.010[f]
Atomic IP	24.587[g]	21.565[g]	15.760[g,h]	14.000[g,i]	12.130[g]

a. Reference 9.

b. Reference 7.

c. P. M. Dehmer and S. T. Pratt, J. Chem. Phys. 76, 843 (1982).

d. Reference 8.

e. Reference 5.

f. C. Y. Ng, D. J. Trevor, B. H. Mahan, and Y. T. Lee, J. Chem. Phys. 65, 4327 (1976).

g. Reference 35.

h. K. Yoshino, J. Opt. Soc. Am. 60, 1220 (1970).

i. K. Yoshino and Y. Tanaka, J. Opt. Soc. Am. 69, 159 (1978).

Table II. Dissociation Energies of the Rare Gas Dimers (cm^{-1})[a]

	He	Ne	Ar	Kr	Xe
He	——	1.9	8.2	7.0	8.3
Ne		17.3[b]	35.9	38.7	39.1
Ar			84.0[c]	100.6	115.3
Kr				126.8[d]	148.3
Xe					185.2[e]

[a] For all of the heteronuclear diatomic molecules, the tabulated values are from Bobetic and Barker, J. Chem. Phys. 64, 2367 (1976).

[b] D. E. Freeman, K. Yoshino, and Y. Tanaka, J. Chem. Phys. 67, 3462 (1977).

[c] R. J. LeRoy, J. Chem. Phys. 57, 573 (1972).

[d] Y. Tanaka, K.Yoshino, and D. E. Freeman, J. Chem. Phys. 59, 5160 (1973).

[e] D. E. Freeman, K. Yoshino, and Y. Tanaka, J. Chem. Phys. 61, 4880 (1974).

Table III. Ground State Dissociation Energies of the Rare Gas Dimer Ions (eV)

	He	Ne	Ar	Kr	Xe
He	2.365 ± 0.006[a]	0.692 ± 0.037[b]	0.026 ± 0.002[c]		
Ne		1.36 ± 0.05[d]	0.079 ± 0.004[e]	0.055 ± 0.003[e]	0.041 ± 0.004[e]
Ar			1.269 ± 0.017[f]	0.528 ± 0.015[g]	0.176 ± 0.012[g]
Kr				1.150 ± 0.004[h]	0.385 ± 0.011[g]
Xe					1.03 ± 0.01[i]

a. Reference 12, p. 298.

b. Reference 14.

c. Reference 15.

d. Reference 9.

e. Reference 7.

f. P. M. Dehmer and S. T. Pratt, J. Chem. Phys. 76, 843 (1982).

g. Reference 8.

h. Reference 5.

i. C. Y. Ng, D. J. Trevor, B. H. Mahan, and Y. T. Lee, J. Chem. Phys. 65, 4327 (1976).

Table IV. Bands of Ar_2 Between the $Ar^+ \, ^2P^o_{3/2}$ and $^2P^o_{1/2}$ Thresholds

Observed molecular bands			Energetics of the atomic dissociation limit[a]				
λ(Å)	E(eV)	n^*	Assumed Dissociation Limit	λ(Å)	E(eV)	n^*	$(D_0-\Delta)$ (meV)[b,c]
786.048	15.7732	11.80	12d′	782.74	15.8399	11.82	77.0
785.329	15.7877	12.78	13d′	782.02	15.8545	12.82	77.2
784.736	15.7996	13.81	14d′	781.45	15.8660	13.82	76.9
784.278	15.8088	14.79	15d′	780.99	15.8753	14.82	76.9
783.884	15.8168	15.84	16d′	780.62	15.8829	15.82	76.5
783.550	15.8235	16.93	17d′	780.31	15.8892	16.8	76.1
783.251	15.8296	18.12	18d′	780.05	15.8944	17.8	75.3
783.080	15.8330	18.93	19d′	779.84	15.8989	18.8	76.3
782.900	15.8367	19.90	20d′	779.65	15.9026	19.8	76.4
782.705	15.8406	21.16	21d′	779.49	15.9059	20.8	76.8
781.206[d]	15.8710	∞		777.957	15.9373	∞	76.7

[a] The assignments and positions of the atomic Rydberg series are from K. Yoshino, J. Opt. Soc. Am. 60, 1220 (1970).

[b] Calculated using $D_0(Ar_2) = 10.4$ meV from R. J. LeRoy, J. Chem. Phys. 5, 573 (1972).

[c] $\Delta \simeq 15 \pm 10$ meV.

[d] The series limit is taken as the vertical ionization potential of the C $^2\Pi_{1/2u}$ state from Reference 16.

Table V. Bands of ArXe Between the Xe^+ $^2P^o_{3/2}$ and $^2P^o_{1/2}$ Thresholds

Observed molecular bands			Energetics of the atomic dissociation limit				
λ(Å)	E(eV)	n^*	Assumed Dissociation Limit	λ(Å)	E(eV)	n^*	$(D_0-\Delta)^a$ (meV)
998.47	12.4175	3.74	6d′	995.47	12.4549	3.72	52
989.79	12.5264	3.97	8s′	986.07	12.5737	3.97	62
969.78	12.7849	4.74	7d′	966.64	12.8264	4.72	56
965.82	12.8373	4.96	9s′	962.01	12.8881	4.98	65
955.18	12.9803	5.76	8d′	952.24	13.0204	5.72	54
953.17	13.0077	5.96	10s′	949.56	13.0571	5.99	64
946.62	13.0977	6.81	9d′	943.84	13.1363	6.73	53
941.55	13.1682	7.82	10d′	938.67	13.2086	7.73	55
938.21	13.2151	8.80	11d′	935.14	13.2585	8.74	58
935.57	13.2524	9.92	12d′	932.64	13.2940	9.77	56
925.90±0.2	13.3908	∞		922.75	13.4365	∞	60±3

(a) Calculated using D_0(ArXe) = 14.3 meV from M. V. Bobetic and J. A. Barker, J. Chem. Phys. 64, 2367 (1976).

Table VI. Excited State Dissociation Energies of the Rare Gas Dimer Ions (eV)[a]

	He	Ne	Ar	Kr	Xe
He	b	$D_0(A_2\ {}^2\Pi_{1/2}) = 0.0350 \pm 0.001$[c] $D_0(B\ {}^2\Sigma^+) = 0.0363 \pm 0.0001$[c]	$D_0(A_2\ {}^2\Pi_{1/2}) = 0.015 \pm 0.002$[d] $D_0(B\ {}^2\Sigma^+) = 0.156 \pm 0.002$[d]	$D_0\ (B\ {}^2\Sigma^+) = 0.22$[e]	$D_0\ (B\ {}^2\Sigma^+) = 0.28$[e]
Ne			$(D_0-\Delta)(B\ {}^2\Pi_{1/2}) = 0.022 \pm 0.002$[f]	$(D_0-\Delta)(B\ {}^2\Pi_{1/2}) = 0.018 \pm 0.004$[f]	$(D_0-\Delta)(B\ {}^2\Pi_{1/2}) = 0.014 \pm 0.002$[f]
Ar			$D_0(B\ {}^2\Pi_{3/2g}) = 0.14 \pm 0.02$[g] $D_0(C\ {}^2\Pi_{1/2u}) = 0.10 \pm 0.02$[g] $(D_0-\Delta)(C\ {}^2\Pi_{1/2u}) = 0.077 \pm 0.002$[g,h]	$(D_0-\Delta)(D\ {}^2\Sigma^+_{1/2}) = 0.087 \pm 0.004$[i]	$(D_0-\Delta)(B\ {}^2\Pi_{1/2}) = 0.060 \pm 0.003$[i]
Kr				$D_0(B\ {}^2\Pi_{3/2g}) = 0.16 \pm 0.02$[g] $D_0(C\ {}^2\Pi_{1/2u}) = 0.14 \pm 0.02$[g] $(D_0-\Delta)(C\ {}^2\Pi_{1/2u}) = 0.113 \pm 0.002$[g,h]	$(D_0-\Delta)(B\ {}^2\Pi_{1/2}) = 0.14 \pm 0.02$[i] $(D_0-\Delta)(D\ {}^2\Sigma^+_{1/2}) = 0.106 \pm 0.003$[i]
Xe					$D_0(B\ {}^2\Pi_{3/2g}) = 0.18 \pm 0.02$[g] $D_0(C\ {}^2\Pi_{1/2u}) = 0.19 \pm 0.02$[g] $(D_0-\Delta)(C\ {}^2\Pi_{1/2u}) = 0.145 \pm 0.002$[g,h]

Footnotes to Table VI

a. Depending on availability, the vertical (D_0-Δ) and/or adiabatic (D_0) dissociation energies are given. The spectroscopic labels are as shown in Figures 1 and 2, except for HeY. For these molecules, the $A_1\ {}^2\Pi_{3/2}$ and $A_2\ {}^2\Pi_{1/2}$ excited electronic states dissociate to $He({}^1S_0) + Y^+({}^2P^o_{1/2})$ and the $B\ {}^2\Sigma^+$ excited electronic state dissociates to $He^+({}^2S_{1/2}) + Y({}^1S_0)$.

b. The single excited state of He_2^+ is repulsive except for a very small van der Waals minimum at 5.3 Å. See Reference 12, p. 298.

c. Reference 14.

d. Reference 15.

e. H. P. Weise, Ber. Bunsenges. Phys. Chem. 77, 578 (1973).

f. Reference 7.

g. Reference 16.

h. Reference 6.

i. Reference 8.

Table VII. Evaluation of the Ion-Induced Dipole Potential at R_e of the Neutral Dimers

Molecule	R_e(Å)	α(Å^3)[a]	$V = \frac{-e^2\alpha}{2R_e^4}$ (meV)	Ionic Convergence Limit	$(D_0-\Delta)$(meV)
NeAr	3.43[b]	0.395	21	B $^2\Pi_{1/2}$	22 ± 2[c]
NeKr	3.58[b]	0.395	17	B $^2\Pi_{1/2}$	18 ± 4[c]
NeXe	3.74[b]	0.395	14	B $^2\Pi_{1/2}$	14 ± 2[c]
Ar_2	3.76[d]	1.642	59	C $^2\Pi_{1/2u}$	76.7 ± 0.7[e]
ArKr	3.88[f]	2.480	79	D $^2\Sigma^+_{1/2}$	87 ± 4[g]
ArXe	4.06[f]	1.642	44	B $^2\Pi_{1/2}$	60 ± 3[g]
Kr_2	4.01[h]	2.480	69	C $^2\Pi_{1/2u}$	112 ± 1.5[e]
KrXe	4.18[f]	2.480	59	B $^2\Pi_{1/2}$	140 ± 20[g]
KrXe	4.18[f]	4.044	95	D $^2\Sigma^+_{1/2}$	106 ± 3[g]
Xe_e	4.36[h]	4.044	81	C $^2\Pi_{1/2u}$	145 ± 1.5[e]

a. A. Dalgarno and A. E. Kingston, Proc. Roy. Soc. (London) A 259, 424 (1960); Proc. Phys. Soc. (London) 78, 607 (1961).

b. C. Y. Ng, Y. T. Lee, and J. A. Barker, J. Chem. Phys. 61, 1996 (1974).

c. Reference 7.

d. R. J. LeRoy, J. Chem. Phys. 57, 573 (1972).

e. Reference 6.

f. D. E. Freeman, K. Yoshino, and Y. Tanaka, J. Chem. Phys. 67, 3462 (1977).

g. Reference 8.

h. J. A. Barker, R. O. Watts, J. K. Lee, T. P. Schafer, and Y. T. Lee, J. Chem. Phys. 61, 3081 (1974).

Table VIII. Bands of Ar_2 Between 822 and 826 Å [a]

		Tentative Assignments			
λ(Å)	ν (cm^{-1})	v′	v″	$\Delta G_{v''+1/2}$ (cm^{-1})	$\Delta G_{v'+1/2}$ (cm^{-1})
822.762	121541.8	v	0		44.3
823.062	121497.5	v-1	0		68.9
823.529	121428.6	v-2	0		70.8
824.010	121357.8	v-3	0		71.6
824.496	121286.2	v-4	0	25.1	71.7
824.667	121261.1		1		
824.984	121214.5	v-5	0		104.5
825.696	121110.0	v-6	0		82.4
826.258	121027.6	v-7	0		

[a] The wavelength scale is accurate to ±0.02 Å; differences are accurate to ±0.005 Å.

Table IX. Energy Levels and Franck-Condon Factors for the Transition Ar_2 $X^1\Sigma_g^+$, $v'' = 0 \rightarrow Ar_2^+$ $B^2\Pi_{3/2g}$, v'

v'	$E_{v'}$ (cm^{-1})	$\Delta G_{v'+1/2}$ (cm^{-1})	FCF
0	0		0.0007
1	111.4	111.4	0.0058
2	218.5	107.2	0.0241
3	320.6	102.1	0.0659
4	416.9	96.2	0.1300
5	506.8	89.9	0.1927
6	589.9	83.1	0.2171
7	666.1	76.2	0.1836
8	735.4	69.3	0.1143
9	797.4	62.0	0.0502
10	851.4	54.0	0.0139
11	896.2	44.8	0.0016

Table X. Bands of KrXe Between 925 and 940 Å.

λ(Å)	ν(cm^{-1})	Δν(cm^{-1})
937.484	106668.5	
		57.1
936.982	106725.6	
		54.0
936.508	106779.6	
		48.3
936.085	106827.9	
		53.3
935.618	106881.2	
		51.0
935.172	106932.2	
		70.8
934.553	107003.0	
		65.9
933.978	107068.9	
		60.3
933.451	107129.2	
		55.2
932.972	107184.4	
		56.2
932.483	107240.6	
		55.5
932.000	107296.1	
		57.1
931.505	107353.2	
		50.2
931.069	107403.4	
		49.3
930.642	107452.7	
		50.1
930.208	107502.8	
		43.3
929.834	107546.1	

Figure Captions

Figure 1. Schematic potential energy curves for the homonuclear rare gas dimer ions.

Figure 2. Schematic potential energy curves for the heteronuclear rare gas dimer ions.

Figure 3. Top view of the ionization and detection regions of the photoionization mass spectrometer, showing (1) lamp housing, (2) monochromator entrance slit, (3) differential pumping assembly for the lamp, (4) monochromator body, (5) exit slit assembly, (6) exit slit adjust mechanism, (7) gridded cage defining the ionization region, (8) ion repeller plate, (9) ion focusing lenses, (10) aluminum oxide photodiode, (11) quadrupole mass filter and housing, (12) channeltron electron multiplier and housing, (13) differential pumping septum, (14) main vacuum chamber, and (15) detector vacuum chamber.

Figure 4. Dependence of the Ar_n^+ ion signal on nozzle stagnation pressure. The data were taken at a wavelength of 772.5 Å with a resolution of 0.45 Å using pure argon expanded at room temperature through a 10 μm diameter nozzle.

Figure 5. Relative photoionization cross section for Ar_2^+ near threshold taken at a wavelength resolution of 0.45 Å. The Ar_2 was produced in a supersonic molecular beam expansion of pure argon at room

temperature using a 12 μm diameter jet and nozzle stagnation pressures of 3.06 atm (lower frame) and 10.16 atm (upper frame). The region from 852-866 Å in each frame is shown expanded by a factor of ten; the baseline of the expanded portions has been shifted to keep the figure compact.

Figure 6. Relative photoionization cross section for Kr_2 taken at a wavelength resolution of 0.45 Å in the region near the ionization threshold.

Figure 7. Relative photoionization cross sections for Ar, NeAr, Ar_2, and ArKr in the energy region between the Ar fine-structure thresholds. The wavelength resolution is 0.28 Å for the ArKr spectrum and 0.15 Å for the remaining spectra.

Figure 8. Relative photoionization cross sections for Kr, NeKr, Kr_2, and KrXe in the energy region between the Kr fine-structure thresholds. The wavelength resolution is 0.28 Å for all the spectra.

Figure 9. Relative photoionization cross sections for Xe, NeXe, ArXe, and Xe_2 in the energy region between the Xe fine-structure thresholds. The wavelength resolution is 0.45 Å for Xe_2 and 0.28 Å for the remaining systems.

Figure 10. Relative photoionization cross sections for NeAr, NeKr, and NeXe in the region of the Ne 3s and 3s′ resonance transitions. The

wavelength resolution is 0.15 Å for NeAr and 0.28 Å for NeKr and NeXe.

Figure 11. Relative photoionization cross sections for NeAr obtained with a supersonic molecular beam source (upper frame) and an effusive molecular beam source (lower frame) at a wavelength resolution of 0.15 Å. The dimer concentration in the spectra obtained with the effusive source is negligible, and $NeAr^+$ is produced solely by associative ionization.

Figure 12. Example of the potential energy curves for NeY and NeY^* that were used in the model calculations described in the text.

Figure 13. Experimental and calculated (solid line) relative photoionization cross sections near the neon $3s'[1/2]_1^o$ resonance transition.

Figure 14. Relative photoionization cross sections for ArKr and ArXe in the region of the Ar^* 5s and 3d transitions taken at a wavelength resolution of 0.28 Å.

Figure 15a. Relative photoionization cross sections for Ar_2, ArKr, and ArXe in the wavelength region from 800 to 825 Å taken at a wavelength resolution of 0.15 Å.

Figure 15b. Relative photoionization cross sections for Ar_2, ArKr, and ArXe in the wavelength region from 825 to 850 Å taken at a wavelength resolution of 0.15 Å.

Figure 16. Relative photoionization cross section for Ar_2 taken at a wavelength resolution of 0.07 Å in the region from 118800 to 119650 cm^{-1}. All of the atomic Ar energy levels are shown in the figure, with those that are optically allowed indicated by the heavy lines. The atomic transitions are shifted in energy with respect to the molecular transitions by an amount equal to D_0 of the Ar_2 ground state. This places the atomic and molecular treansitions on the same energy scale assuming that all of the molecular transitions originate in $v'' = 0$ of the ground state.

Figure 17. Relative photoionization cross section for KrXe in the wavelength region from 925 to 940 Å taken at a wavelength resolution of 0.15 Å.

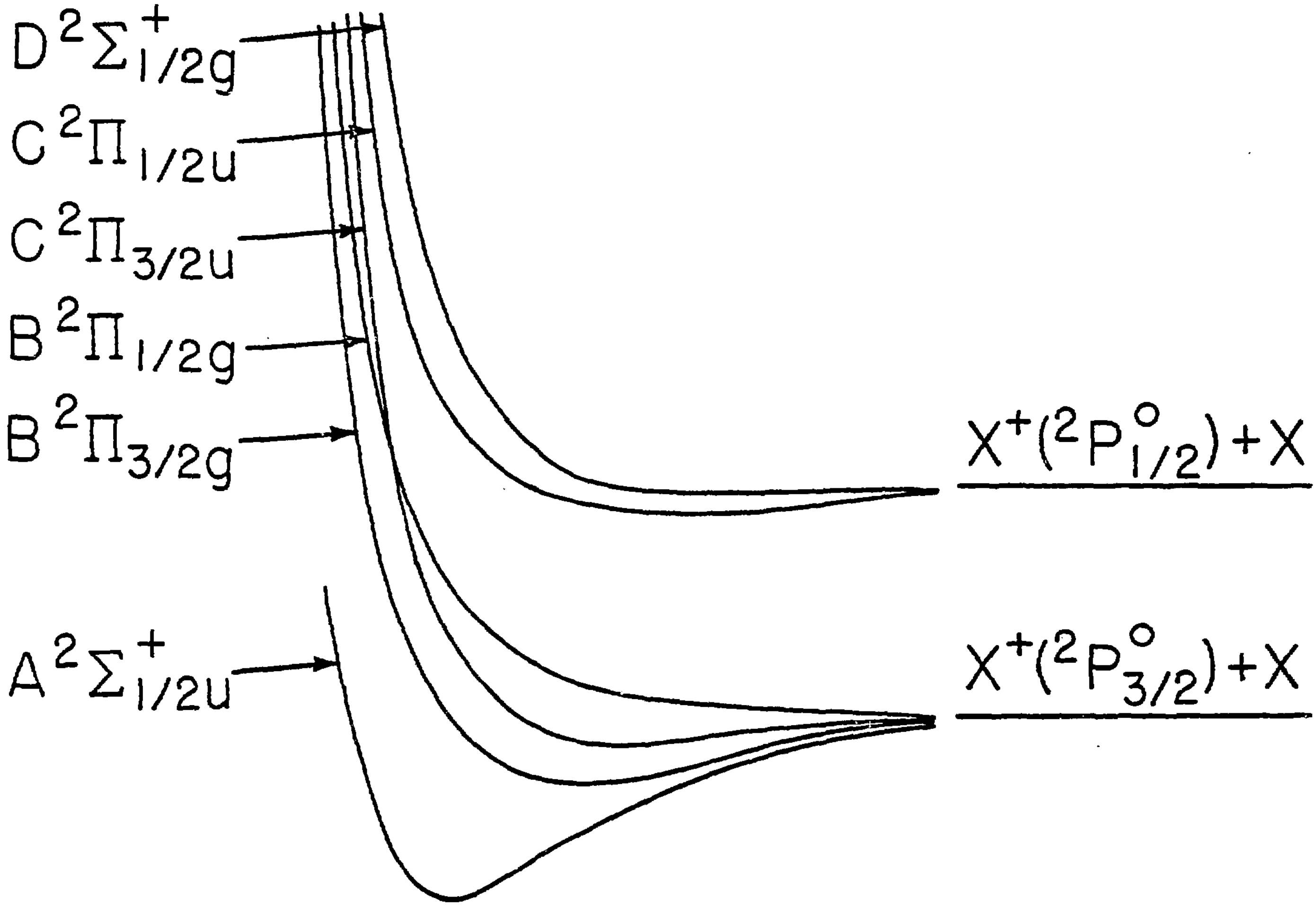
$D^2\Sigma^+_{1/2g}$
$C^2\Pi_{1/2u}$
$C^2\Pi_{3/2u}$
$B^2\Pi_{1/2g}$
$B^2\Pi_{3/2g}$
$A^2\Sigma^+_{1/2u}$
$X^+(^2P^o_{1/2})+X$
$X^+(^2P^o_{3/2})+X$

FIGURE 1

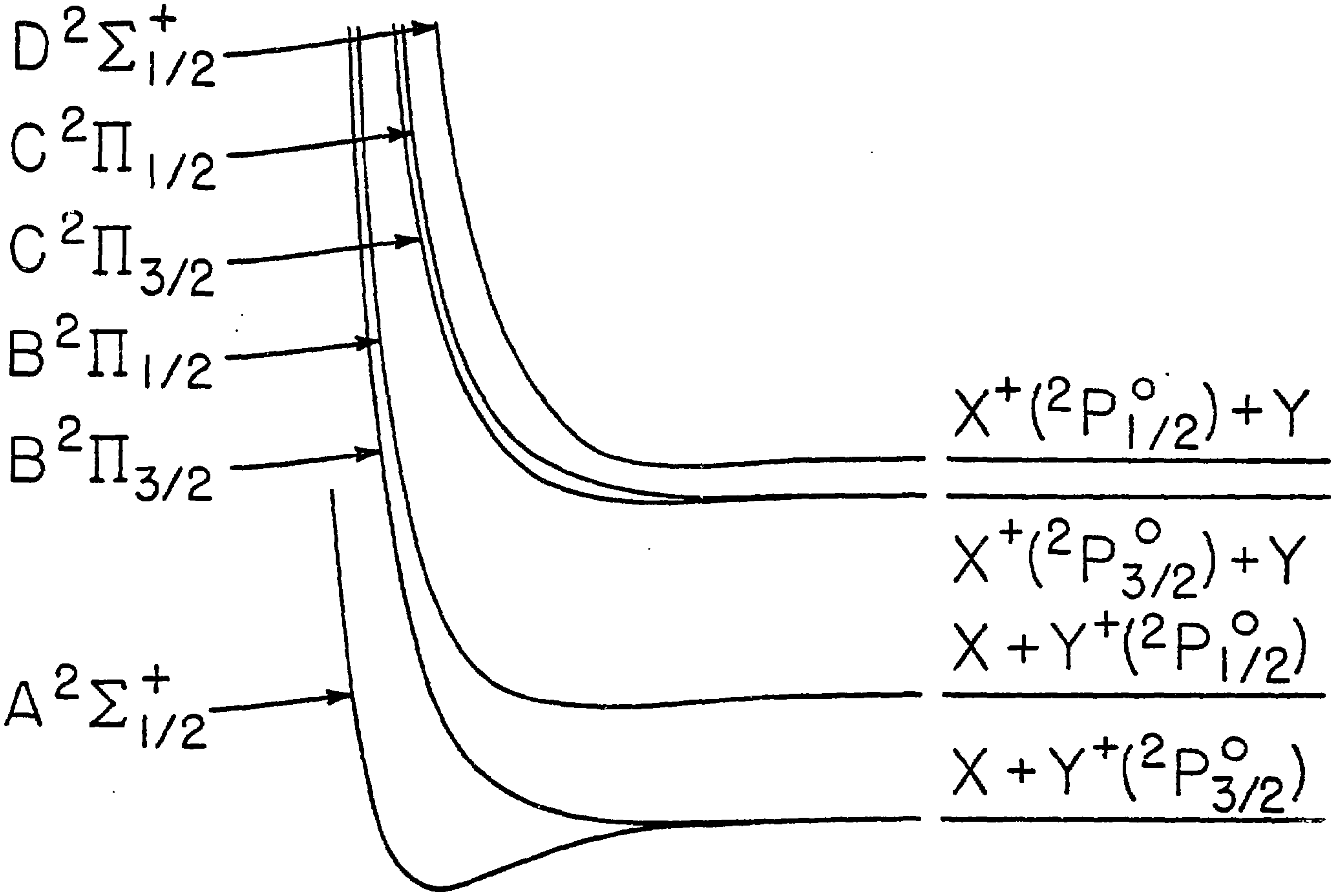
$D\,^2\Sigma^+_{1/2}$
$C\,^2\Pi_{1/2}$
$C\,^2\Pi_{3/2}$
$B\,^2\Pi_{1/2}$
$B\,^2\Pi_{3/2}$
$A\,^2\Sigma^+_{1/2}$
$X^+(^2P^o_{1/2})+Y$
$X^+(^2P^o_{3/2})+Y$
$X+Y^+(^2P^o_{1/2})$
$X+Y^+(^2P^o_{3/2})$

FIGURE 2

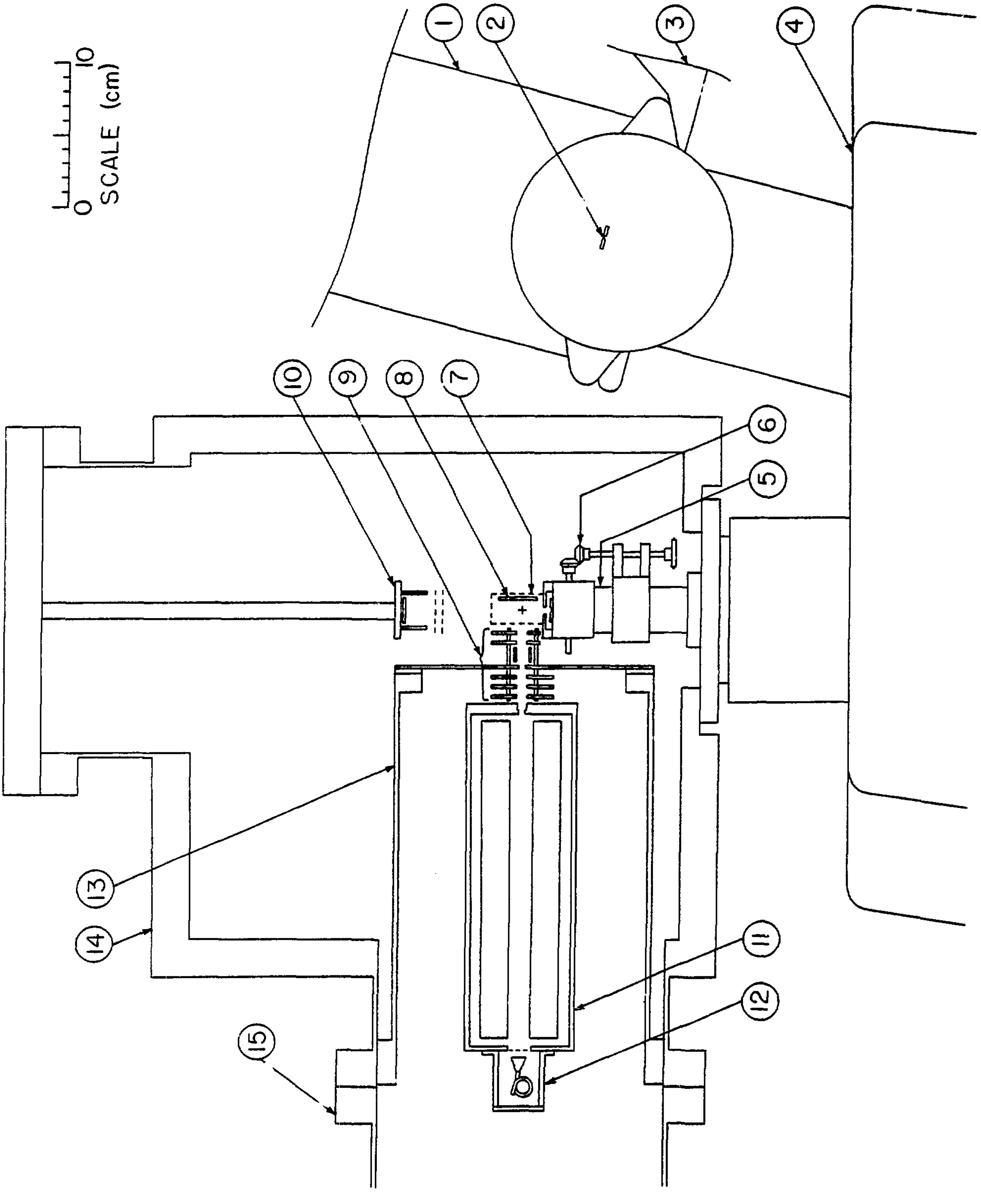

FIGURE 3

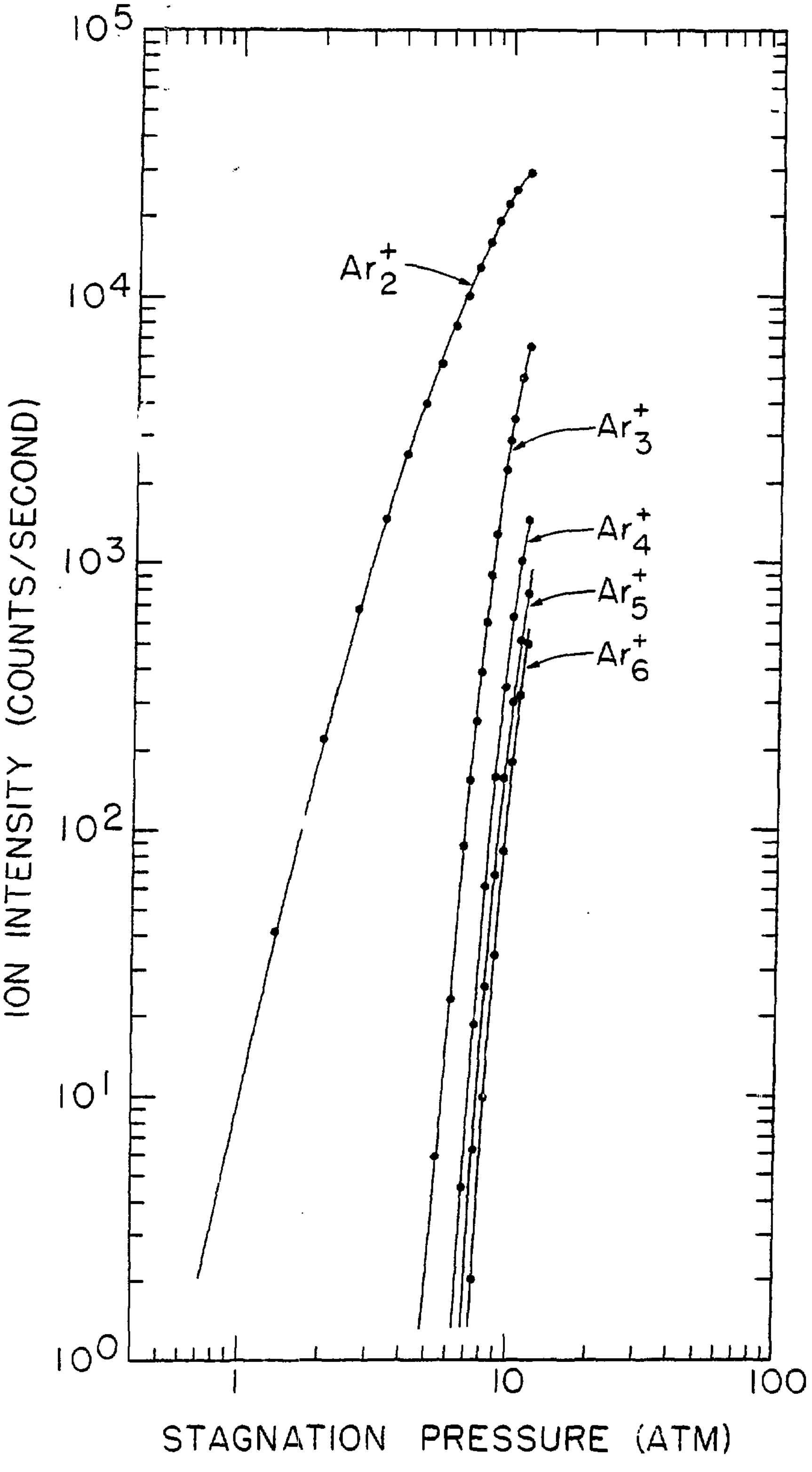

10^5
10^4
10^3
10^2
10^1
10^0
ION INTENSITY (COUNTS/SECOND)
Ar_2^+
Ar_3^+
Ar_4^+
Ar_5^+
Ar_6^+
1
10
100
STAGNATION PRESSURE (ATM)

FIGURE 4

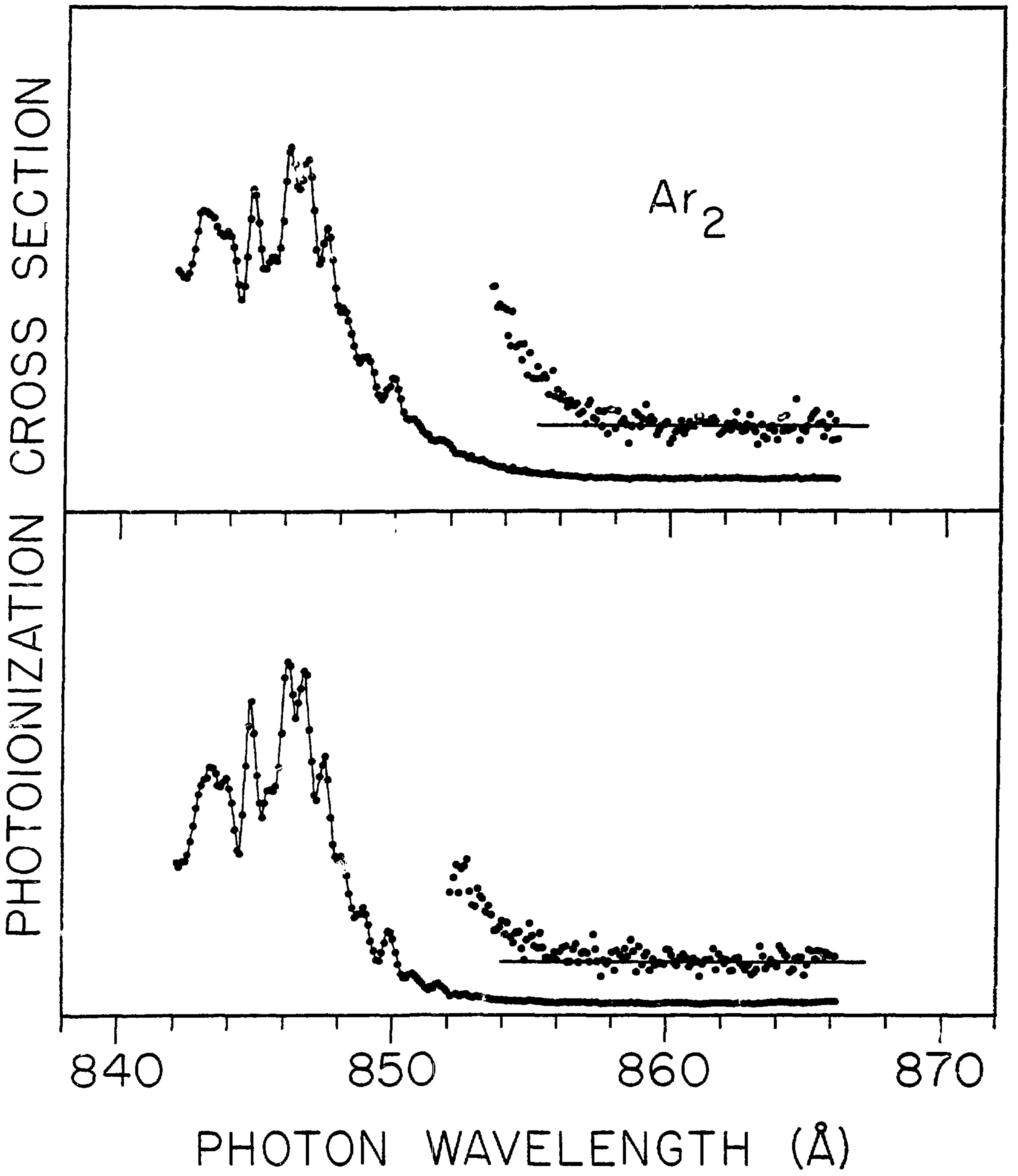
Ar2
PHOTOIONIZATION CROSS SECTION
840
850
860
870
PHOTON WAVELENGTH (Å)

FIGURE 5

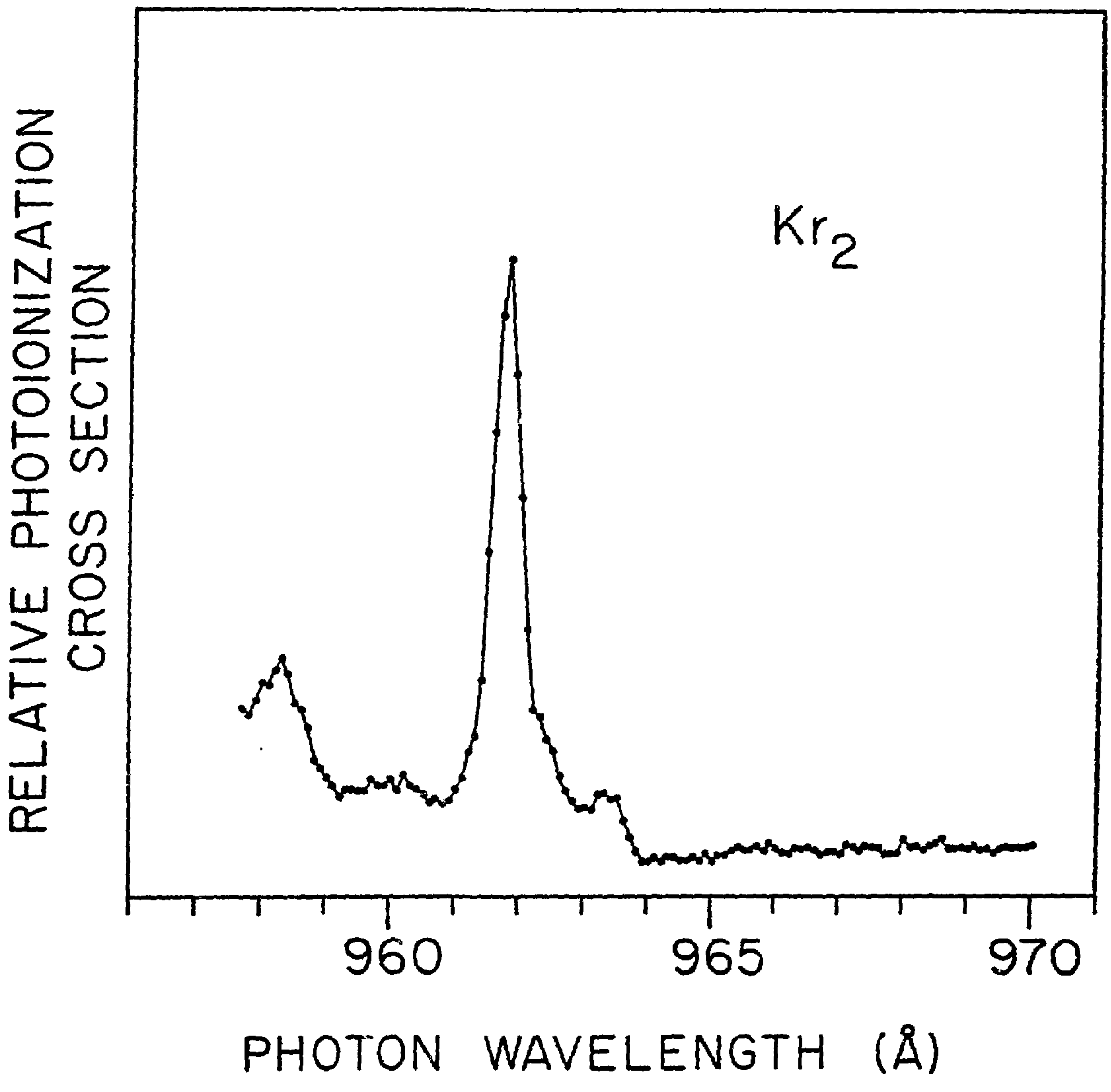
RELATIVE PHOTOIONIZATION CROSS SECTION
Kr$_2$
960
965
970
PHOTON WAVELENGTH (Å)

FIGURE 6

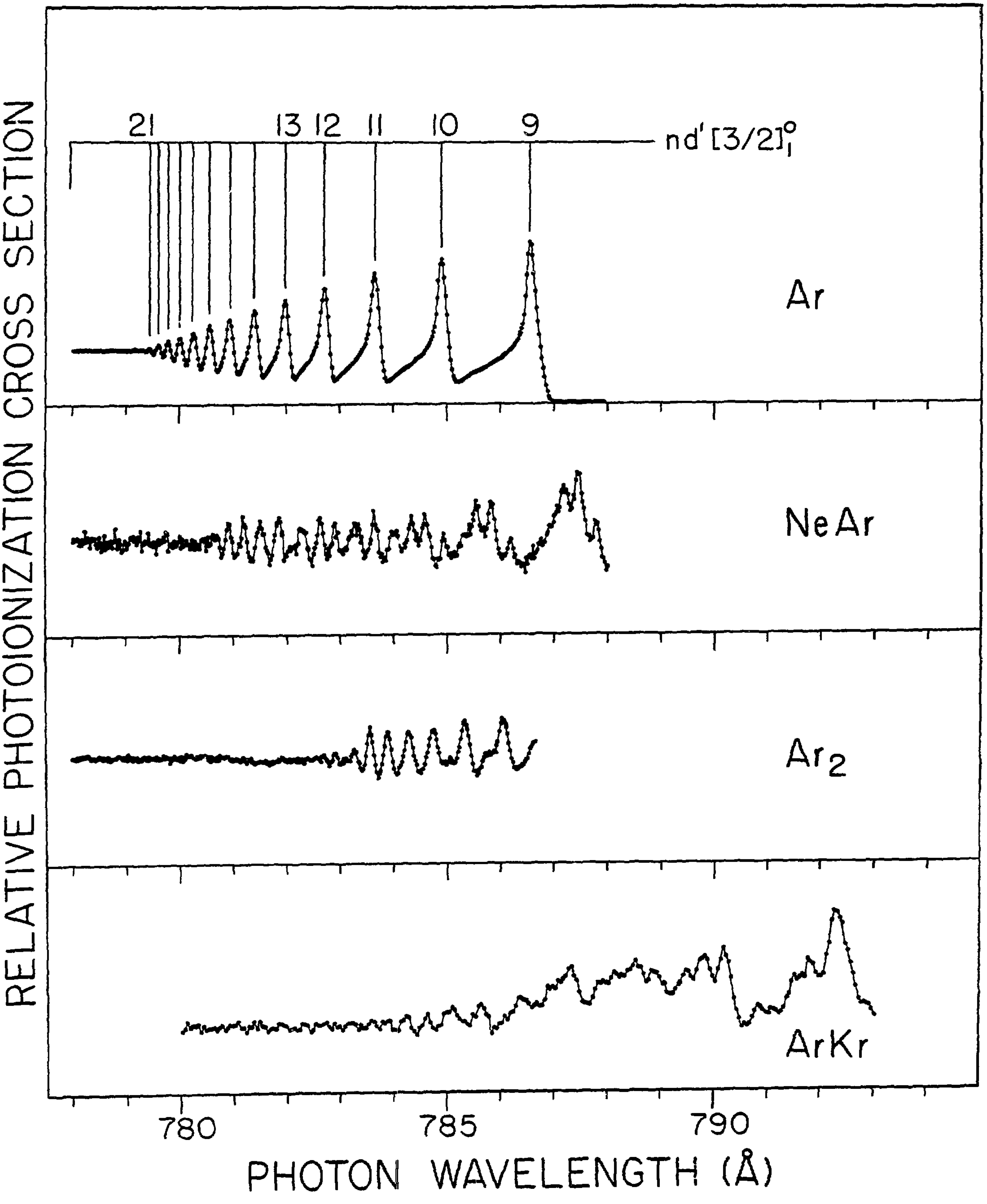
RELATIVE PHOTOIONIZATION CROSS SECTION
21
13
12
11
10
9
nd'$[3/2]_1^o$
Ar
NeAr
Ar_2
ArKr
780
785
790
PHOTON WAVELENGTH (Å)

FIGURE 7

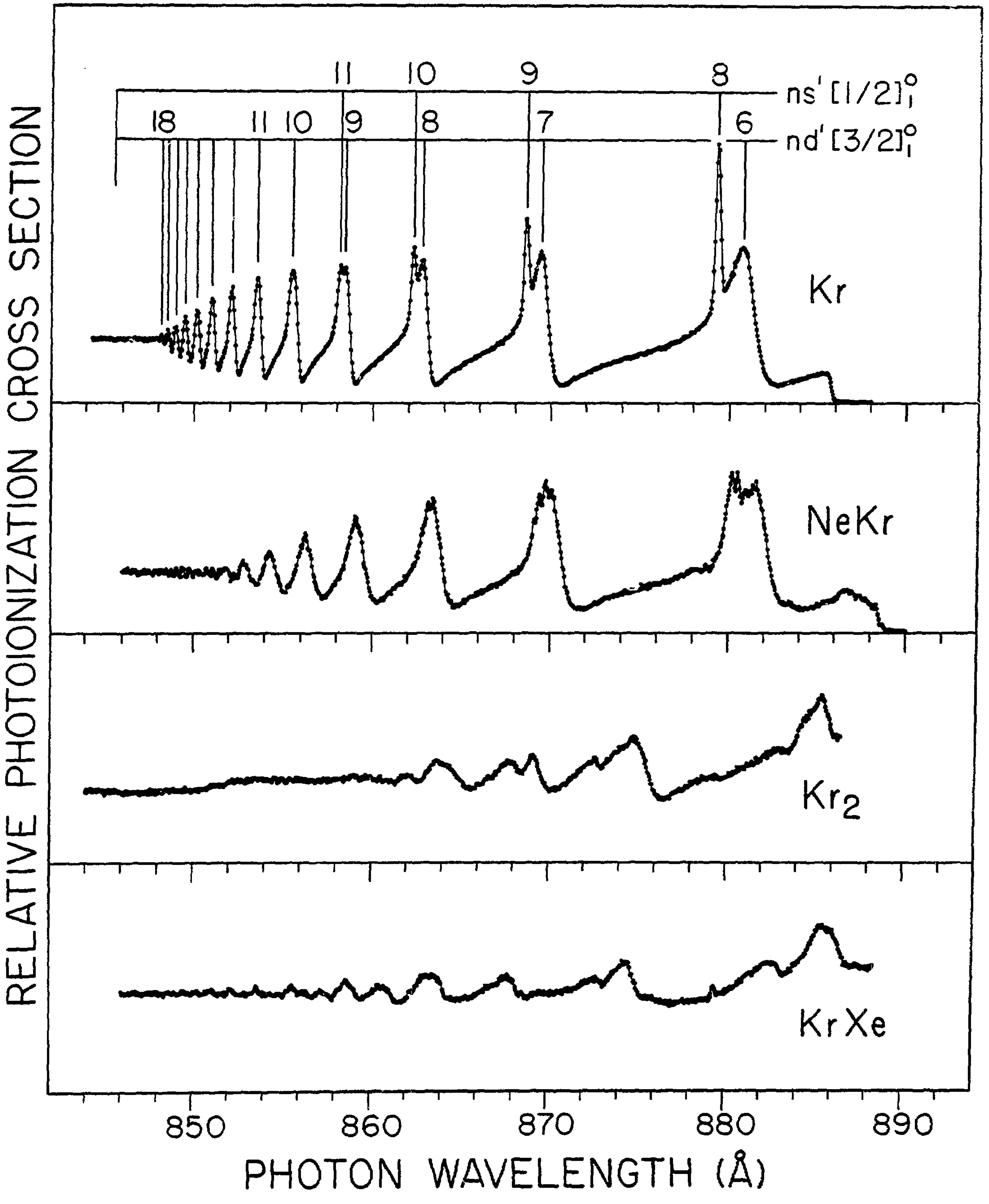
RELATIVE PHOTOIONIZATION CROSS SECTION
PHOTON WAVELENGTH (Å)
850
860
870
880
890
11
10
9
8
ns' [1/2]°₁
18
11
10
9
8
7
6
nd' [3/2]°₁
Kr
NeKr
Kr₂
Kr Xe

FIGURE 8

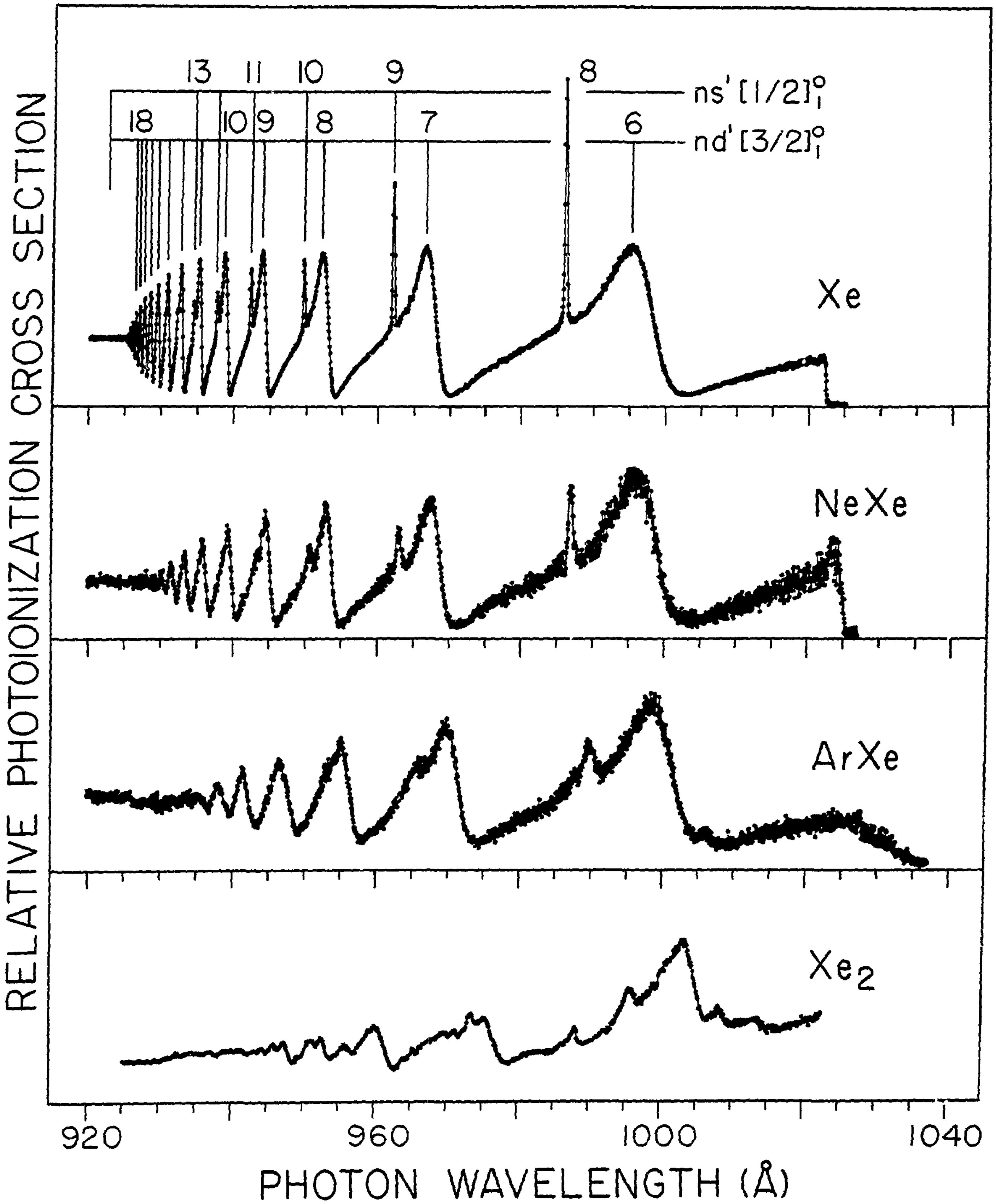

RELATIVE PHOTOIONIZATION CROSS SECTION
13
11
10
9
8
ns' [1/2]$^{o}_{1}$
18
10
9
8
7
6
nd' [3/2]$^{o}_{1}$
Xe
NeXe
ArXe
Xe$_2$
920
960
1000
1040
PHOTON WAVELENGTH (Å)

FIGURE 9

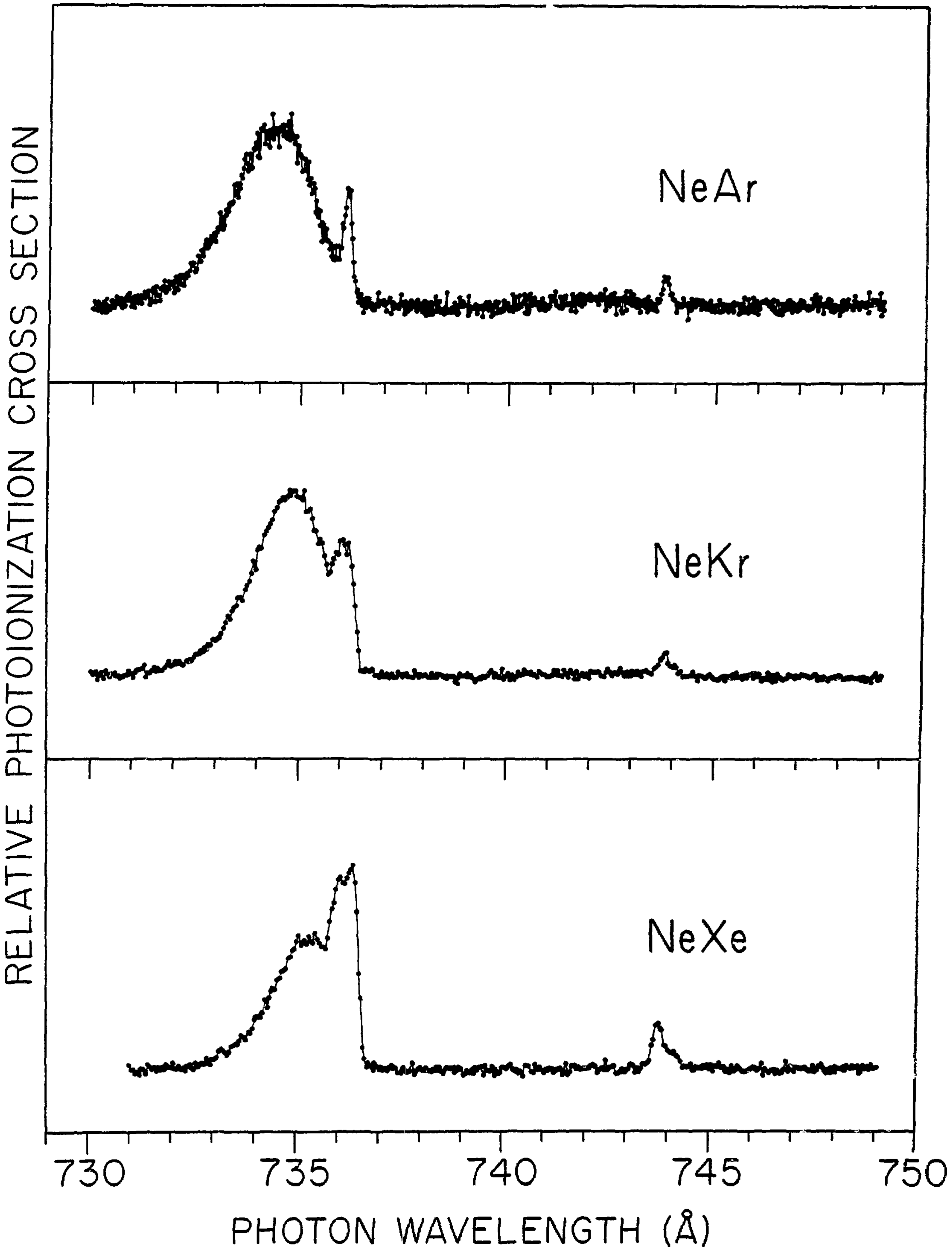
RELATIVE PHOTOIONIZATION CROSS SECTION
NeAr
NeKr
NeXe
730
735
740
745
750
PHOTON WAVELENGTH (Å)

FIGURE 10

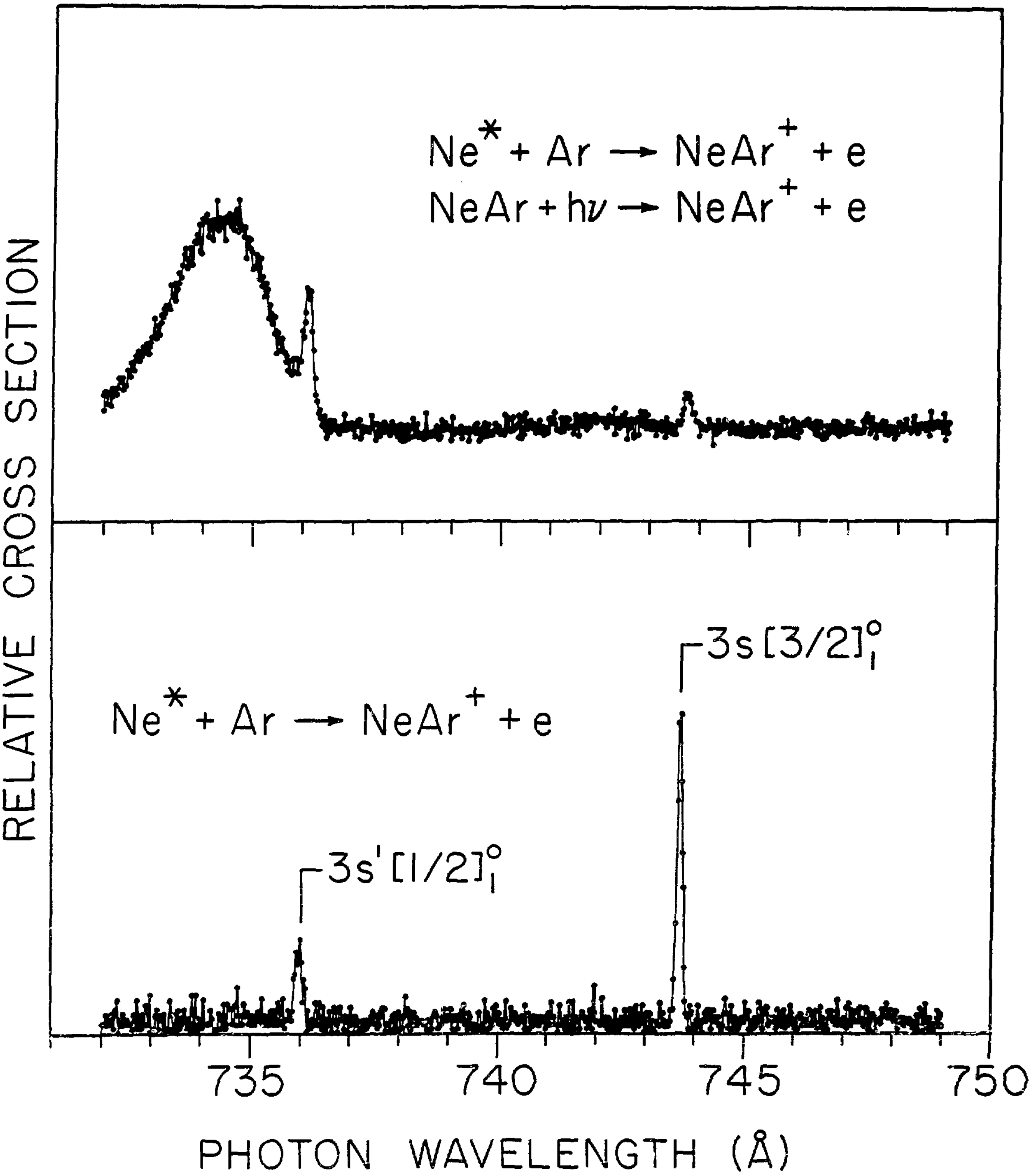
Ne* + Ar → NeAr+ + e
NeAr + hν → NeAr+ + e
Ne* + Ar → NeAr+ + e
3s'[1/2]°1
3s[3/2]°1
RELATIVE CROSS SECTION
735
740
745
750
PHOTON WAVELENGTH (Å)

FIGURE 11

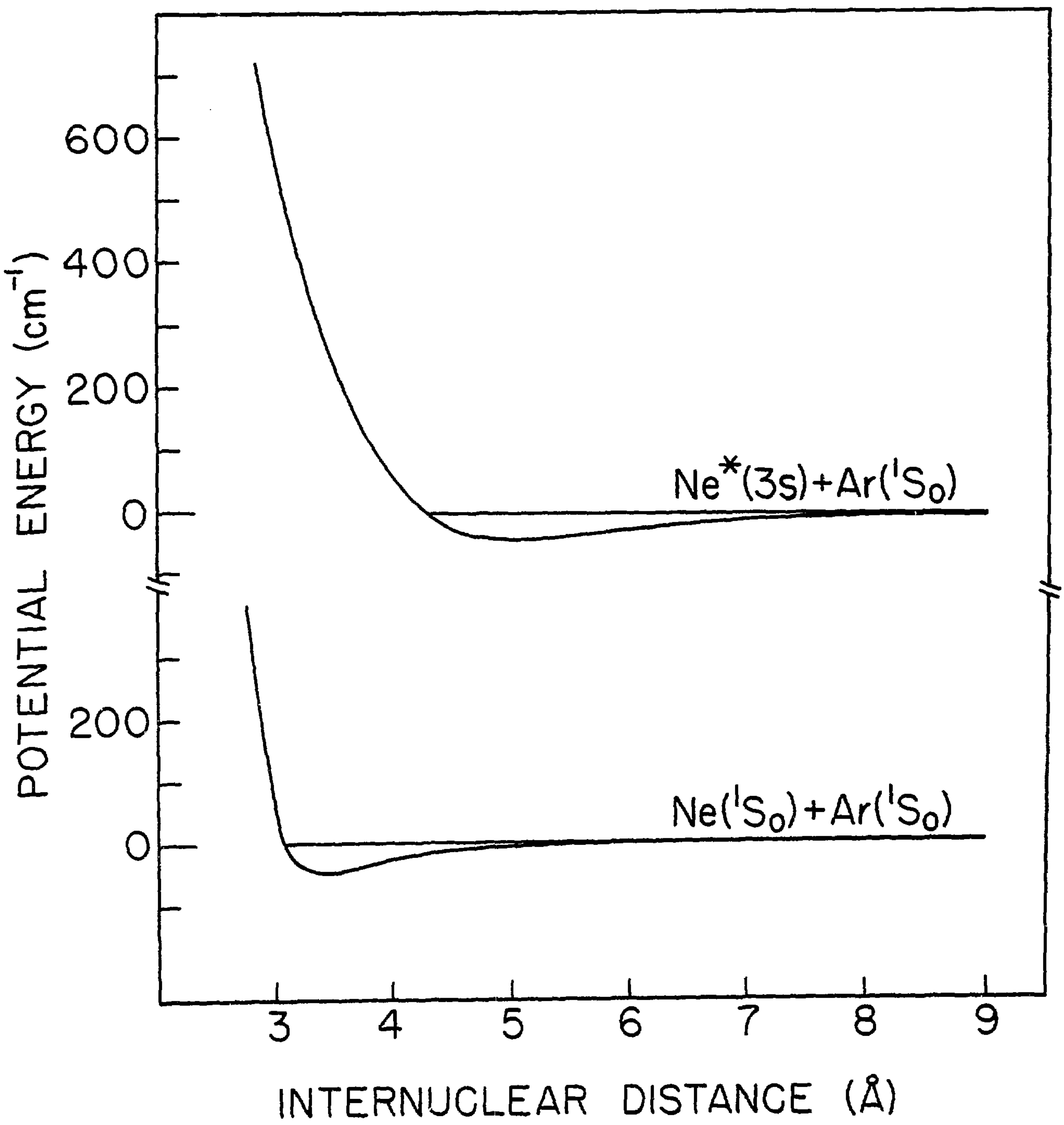POTENTIAL ENERGY (cm^{-1})
600
400
200
0
200
0
Ne*(3s)+Ar($^1S_0$)
Ne($^1S_0$)+Ar($^1S_0$)
3
4
5
6
7
8
9
INTERNUCLEAR DISTANCE (Å)

FIGURE 12

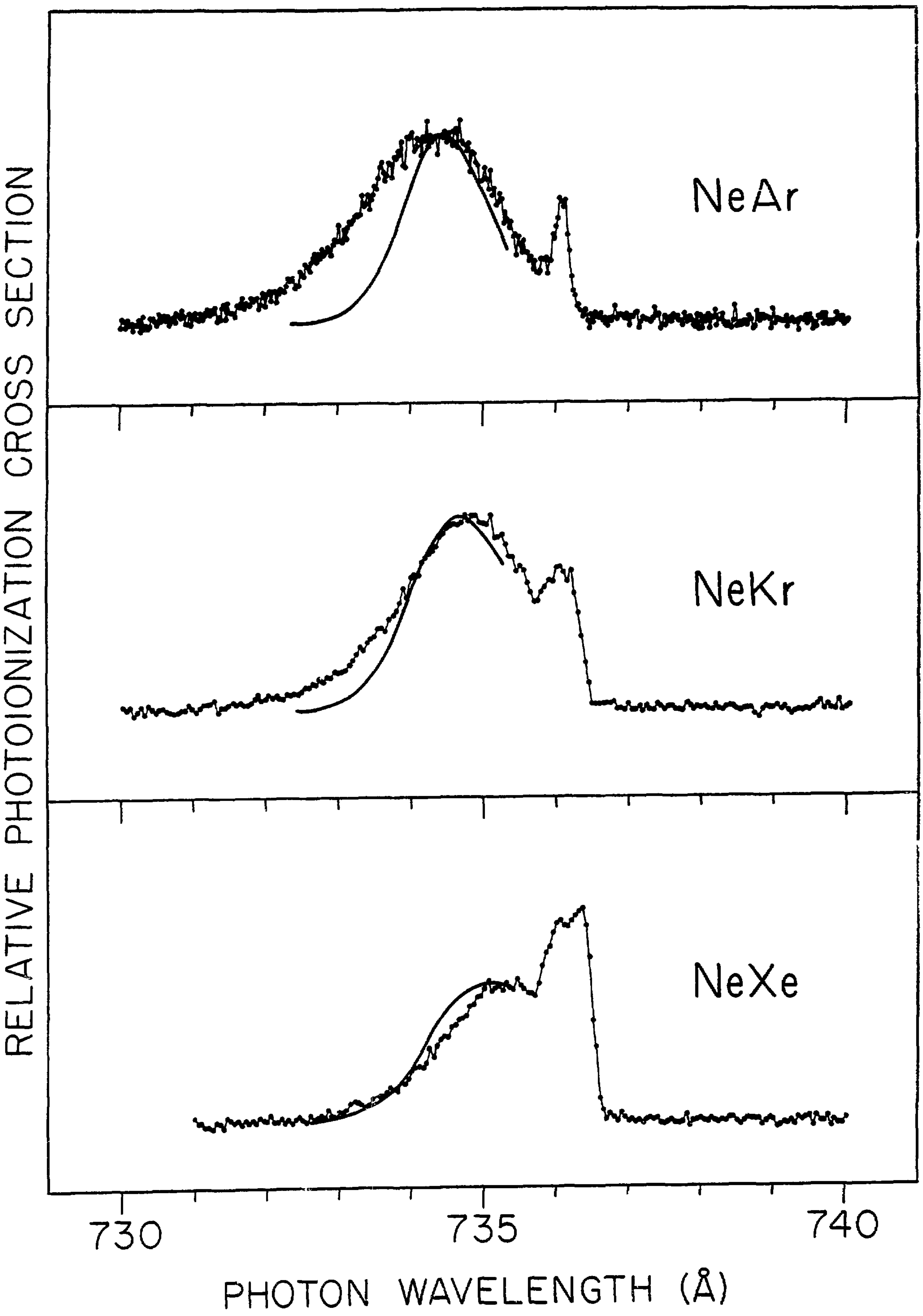
RELATIVE PHOTOIONIZATION CROSS SECTION
NeAr
NeKr
NeXe
730
735
740
PHOTON WAVELENGTH (Å)

FIGURE 13

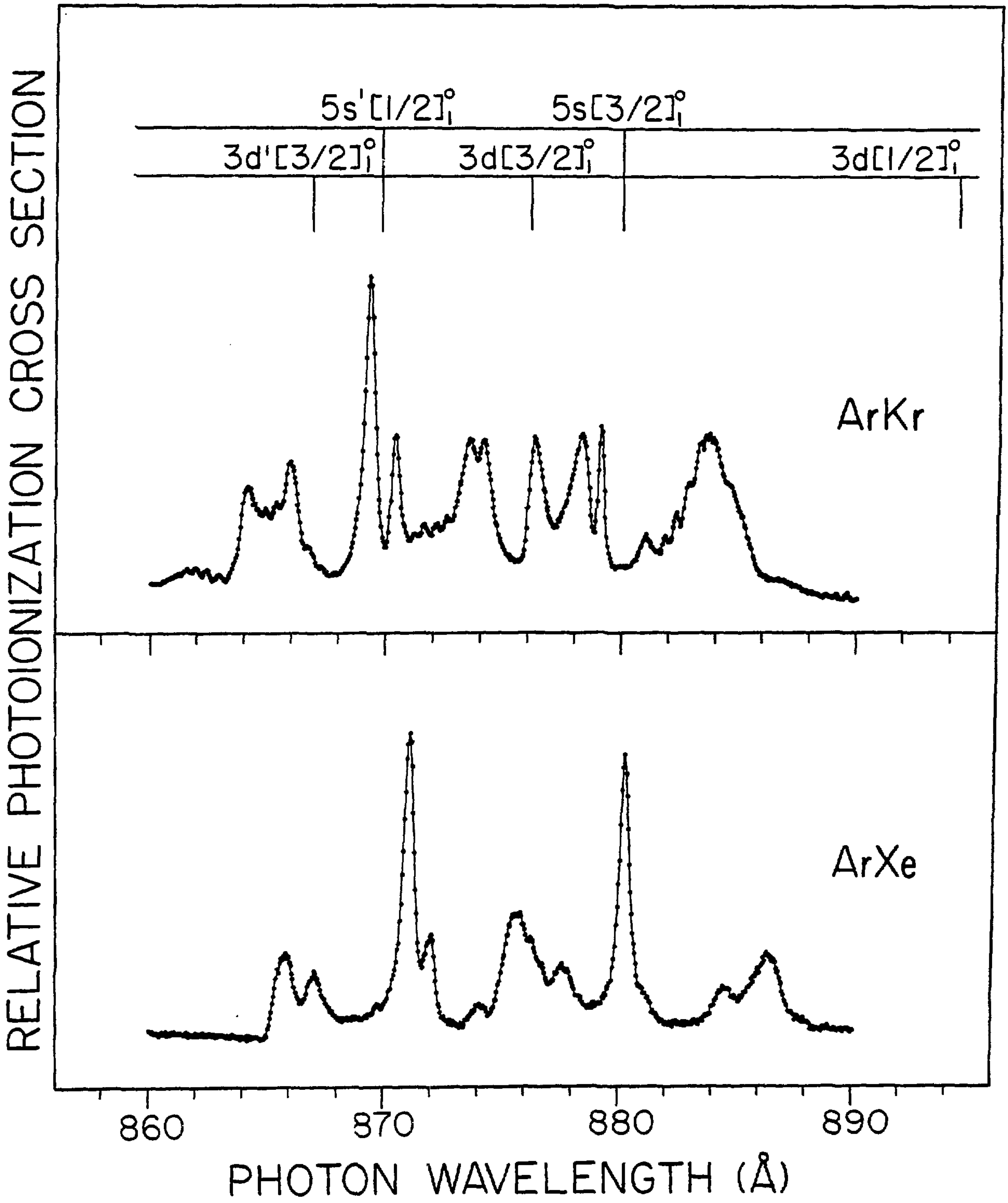
RELATIVE PHOTOIONIZATION CROSS SECTION
5s'[1/2]°₁
5s[3/2]°₁
3d'[3/2]°₁
3d[3/2]°₁
3d[1/2]°₁
ArKr
ArXe
860
870
880
890
PHOTON WAVELENGTH (Å)

FIGURE 14

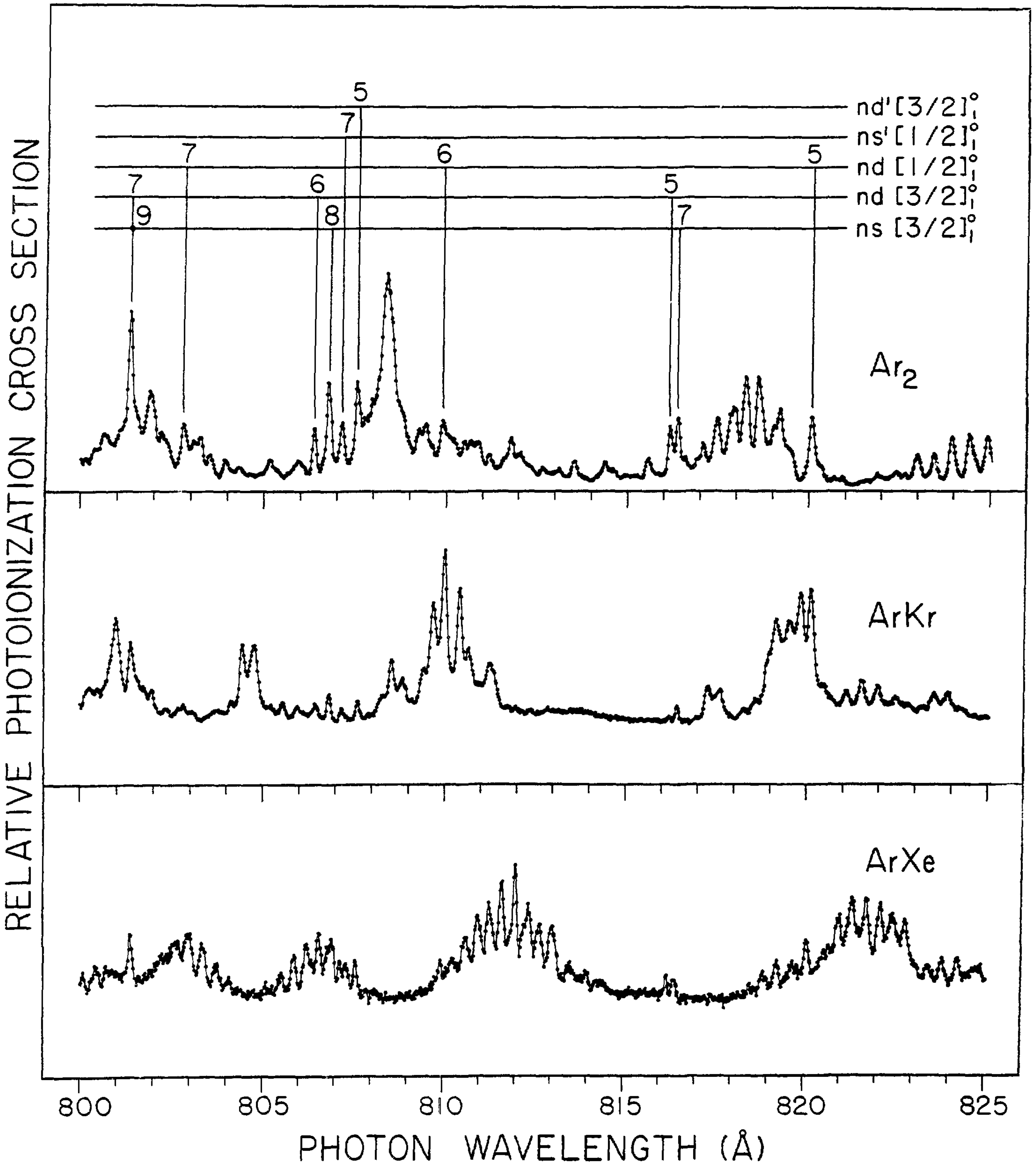
nd'[3/2]$_1^\circ$
ns'[1/2]$_1^\circ$
nd [1/2]$_1^\circ$
nd [3/2]$_1^\circ$
ns [3/2]$_1^\circ$
5
7
7
6
5
7
6
5
9
8
7
Ar$_2$
ArKr
ArXe
RELATIVE PHOTOIONIZATION CROSS SECTION
800
805
810
815
820
825
PHOTON WAVELENGTH (Å)

FIGURE 15a

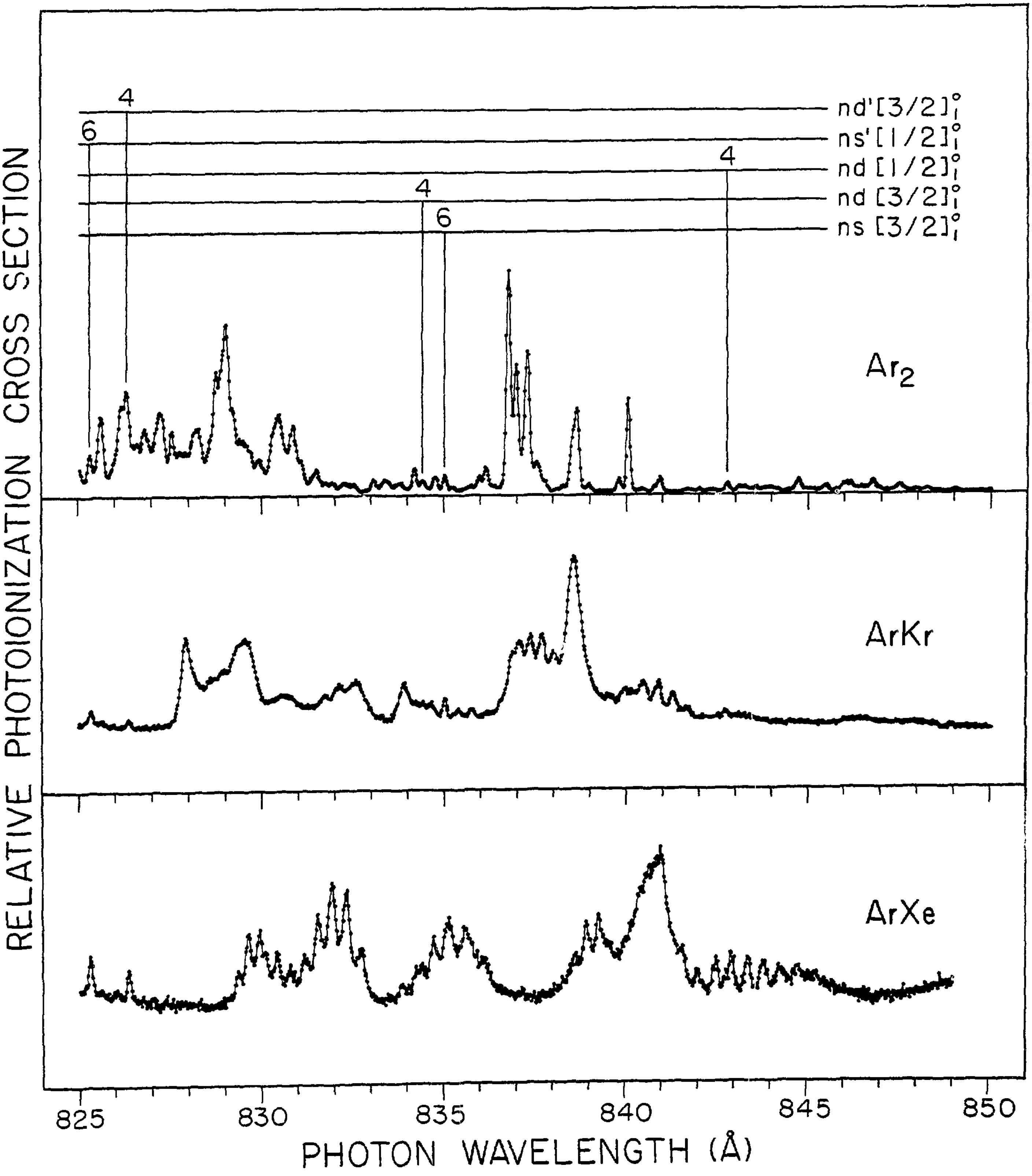
RELATIVE PHOTOIONIZATION CROSS SECTION
nd'[3/2]°₁
ns'[1/2]°₁
nd [1/2]°₁
nd [3/2]°₁
ns [3/2]°₁
6
4
4
6
4
Ar₂
ArKr
ArXe
825
830
835
840
845
850
PHOTON WAVELENGTH (Å)

FIGURE 15b

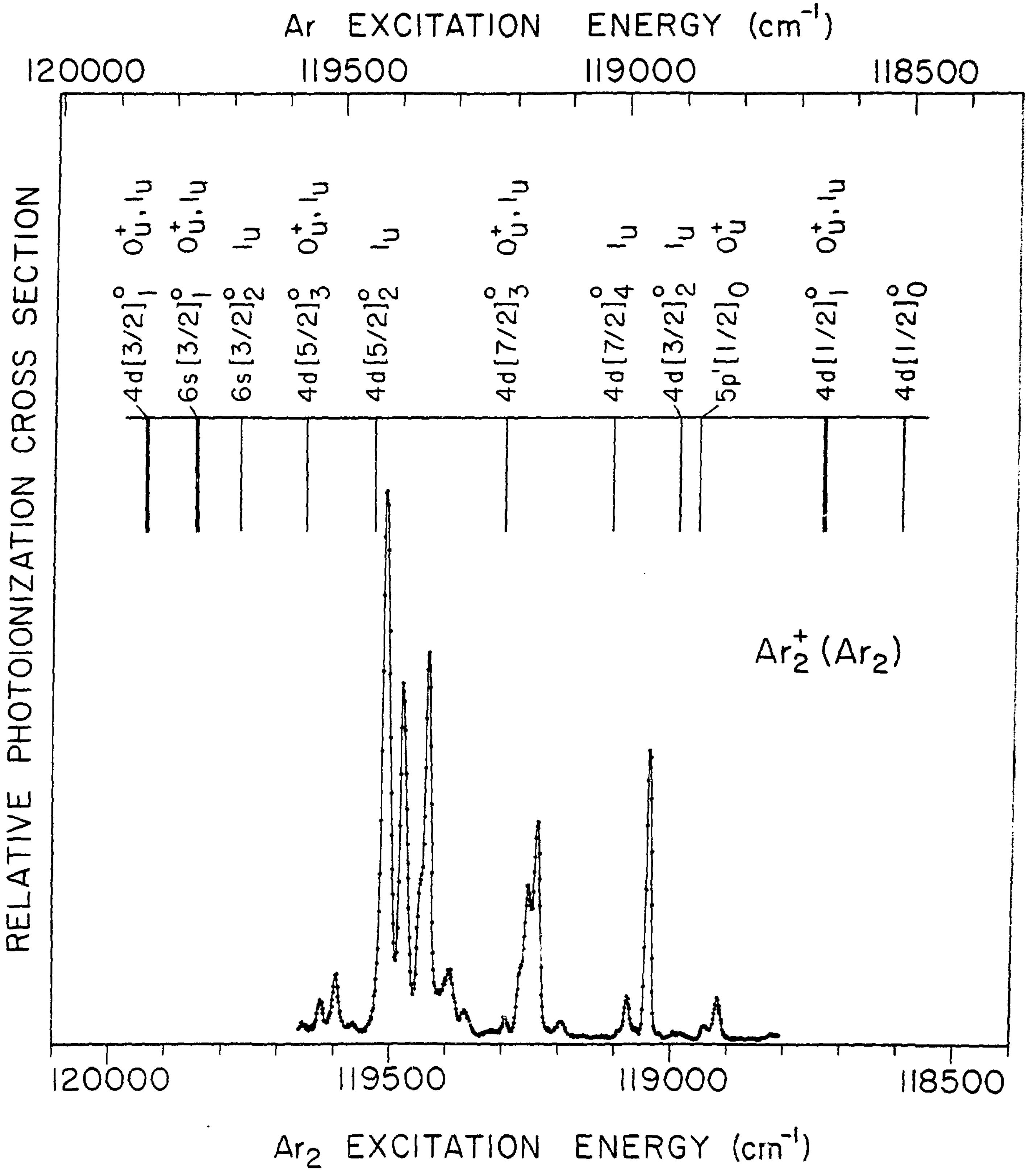
Ar EXCITATION ENERGY (cm^{-1})
120000
119500
119000
118500
RELATIVE PHOTOIONIZATION CROSS SECTION
$4d[3/2]^o_1$ $0_u^+, 1_u$
$6s[3/2]^o_1$ $0_u^+, 1_u$
$6s[3/2]^o_2$ 1_u
$4d[5/2]^o_3$ $0_u^+, 1_u$
$4d[5/2]^o_2$ 1_u
$4d[7/2]^o_3$ $0_u^+, 1_u$
$4d[7/2]^o_4$ 1_u
$4d[3/2]^o_2$ 1_u
$5p'[1/2]_0$ 0_u^+
$4d[1/2]^o_1$ $0_u^+, 1_u$
$4d[1/2]^o_0$
$Ar_2^+ (Ar_2)$
120000
119500
119000
118500
Ar_2 EXCITATION ENERGY (cm^{-1})

FIGURE 16

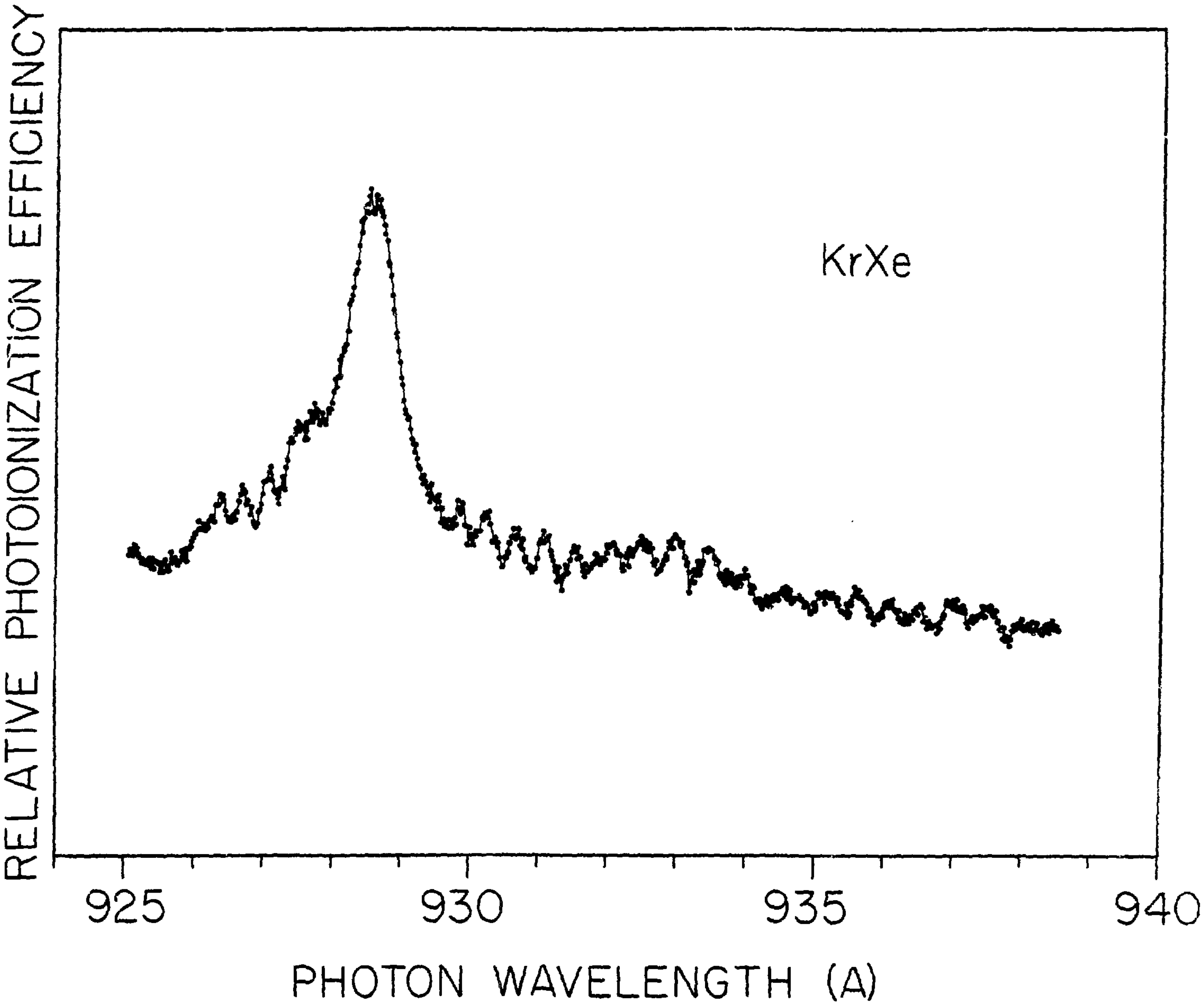

RELATIVE PHOTOIONIZATION EFFICIENCY
KrXe
925
930
935
940
PHOTON WAVELENGTH (A)

FIGURE 17